

# Effect of 3D Structure and Grain Boundaries on Lithium Transport in Garnet Solid Electrolytes

Anton Neumann,<sup>\*,†,‡</sup> Tanner R. Hamann,<sup>¶</sup> Timo Danner,<sup>†,‡</sup> Simon Hein,<sup>†,‡</sup>  
Katharina Becker-Steinberger,<sup>†,‡</sup> Eric Wachsman,<sup>¶</sup> and Arnulf Latz<sup>†,‡,§</sup>

<sup>†</sup>*German Aerospace Center (DLR), Institute of Engineering Thermodynamics,  
Pfaffenwaldring 38-40, 70569 Stuttgart, Germany*

<sup>‡</sup>*Helmholtz Institute for Electrochemical Energy Storage (HIU), Helmholtzstraße 11, 89081  
Ulm, Germany*

<sup>¶</sup>*Maryland Energy Innovation Institute, and Department of Materials Science and  
Engineering, University of Maryland (UMD), College Park MD 20742, USA*

<sup>§</sup>*Ulm University (UUlm), Institute of Electrochemistry, Albert-Einstein-Allee 47, 89081  
Ulm, Germany*

E-mail: anton.neumann@dlr.de

## Abstract

Lithium metal anodes are vital enablers for high energy all-solid-state batteries (ASSBs). To promote ASSBs in practical applications, performance limitations like the high lithium interface resistance and the grain boundary resistance in the solid electrolyte (SE) need to be understood and reduced by optimization of the cell design. In this work, we use our 3D micro-structure resolved simulation approach combined with a modified grain boundary transport model for the SE to shed some light on the

aforementioned limitations in garnet ASSBs. By using high-resolution volume images of the SE electrode sample, we are able to reconstruct the SE microstructure. Using a grain segmentation algorithm, we further distinguish individual grains and account for the influence of the SE grain size and grain boundaries. We focus our simulation work on the trilayer cell architecture, consisting of two porous SE electrodes separated by a dense layer. Even though the highly porous SE electrodes reduce the lithium interface resistance by providing a higher active surface area, the increased electrode tortuosity also reduces the effective ionic conductivity in the SE. We confirm via impedance simulation studies and validation against experimental results that with increasing SE electrode porosity, the lithium transport becomes limited by grain boundaries. We also correlate the area specific resistance to different lithium infiltration stages in the trilayer cell by spatially resolving the current density distribution. This analysis allows us to suggest a plausible deposition mechanism and, moreover, we identify current density hot spots in the proximity of the dense layer. These hot spots might lead to dendrite formation and long-term cell failure. The joint theoretical and experimental study gives guidelines for cell design and optimization which allow further improvement of the trilayer architecture.

## Keywords

all-solid-state batteries, garnet solid electrolyte, 3D microstructure-resolved simulations, interface resistance, grain , lithium interface

## 1 Introduction

All-solid-state batteries (ASSBs) promise very high theoretical energy densities, which is an essential requirement for the electrification of our society.<sup>1,2</sup> The advantages of solid electrolytes (SE) are their reduced flammability and increased safety, which is a prerequisite e.g., for electric vehicles.<sup>3,4</sup> Furthermore, they are seen as an enabler for lithium metal anodes,

which will increase power and energy density. Thereby, garnet type SEs such as  $\text{Li}_7\text{La}_3\text{Zr}_2\text{O}_{12}$  (LLZO) are considered to be almost ideal candidates since they possess high ionic conductivity of more than 0.5 mS/cm and show remarkable electrochemical stability.<sup>5,6</sup> Additionally, garnet type SEs have interesting mechanical properties allowing them to be used as a self-supporting structure during manufacturing.<sup>7</sup> This might allow for new cell designs that can further increase energy density at the cell level.<sup>8,9</sup> Naturally, the application of SEs in conventional cell designs also causes some challenges which need to be addressed.

Liquid electrolytes perfectly wet the surface of the active material (AM), improving the electrochemical reaction environment. With SEs the situation at the interface is more complex and requires interface engineering on the negative<sup>10,11</sup> as well as on the positive electrode.<sup>12-14</sup> Most prominently on the negative electrode, the generally poor contact between the SE and the lithium metal anode results in a large interfacial resistance.<sup>6,15,16</sup> The contact between the two electrodes can also deteriorate due to the Li metal electrode's volume change during plating and stripping, resulting in a constant rise of the cell resistance. One approach is to increase the external pressure on the cells, resulting in a significant reduction of the charge transfer resistance, which causes additional mechanical stress within the cell.<sup>17</sup> Therefore, several authors try to improve the Li-SE interface itself by adding polymeric interlayers<sup>18-20</sup> or by surface chemistry control methods such as coating of lithiophilic layers.<sup>9,21,22</sup>

The separator in LLZO based ASSBs is typically a dense sintered pellet. A major concern of the solid cell system with metallic lithium is the formation of Li dendrites along grain boundaries (GB) in the polycrystalline SE. The emerging dendrites penetrate the cell and lead to cell failure due to short-circuiting.<sup>10,11,23</sup> Thereby, we distinguish between the external and internal origination for dendrite formation. The internal formation of dendrites along GB is facilitated through the low remaining electronic conductivity of LLZO, enabling extended electronic pathways, which eventually reach the GB and reduce the present lithium-ions.<sup>24,25</sup> Moreover, recent atomistic calculations suggest,<sup>26</sup> that the lower band gap of the LLZO surface states compared to the bulk can promote internal dendrite formation.

As for externally originating dendrites surface carbonates that prevent wetting,<sup>9</sup> surface flaws such as scratches, and the defect like nature of GBs and the resulting reduced transport along the GBs are a key aspect.<sup>10,11,27</sup> Combined with the presence of poor interface contact (non-wetting) between lithium metal and the SE, the rise in interface current hot spots initiates a preferential dendrite formation at these surface flaws and along GBs.<sup>28</sup> The often cited empirical "critical current density" (CCD) is generally used to define the highest possible current density before cell failure,<sup>16</sup> originating by either of these processes. Suitable approaches to reduce the formation of internal dendrites are the reduction of the electronic conductivity of the SE or the aforementioned addition of electronically-blocking coatings at the SE surface.<sup>19,22</sup> As for the prevention of external dendrites the optimization of the SE to lithium metal interface is necessary and the recent realization of the importance of this has significantly reduced the interfacial impedance resulting in increased CCD. We demonstrated importance of modifying SE surface to remove lithium carbonate layer by atomic layer deposition (ALD) of thin (5 nm) alumina layer to enable lithium wetting resulting in a reduction of interfacial impedance by over 2 orders of magnitude.<sup>9</sup> Subsequently, it was shown by Taylor *et al.*<sup>21</sup> that the introduction of a thin gold interlayer between LLZO and the lithium metal, essentially doing the same, can significantly increase the room temperature CCD from 0.5 mA/cm<sup>2</sup> up to 0.9 mA/cm<sup>2</sup> compared to a conventional unmodified Li metal electrode.<sup>23</sup> The recent experimental findings emphasize, that in order to enable metallic lithium anodes for commercial high current density and thus high power ASSBs, interface compatibility needs to be improved.

Beyond improving wetting of lithium across the entire SE surface, increasing the total interfacial surface area is critical to increase current density. One possible solution is the so-called trilayer structure proposed by the authors, which is a 3D garnet framework consisting of two highly porous Li<sub>7</sub>La<sub>2.75</sub>Ca<sub>0.25</sub>Zr<sub>1.75</sub>Nb<sub>0.25</sub>O<sub>12</sub> (LLCZNO) layers (~70-100 μm), separated by a thin but highly dense SE layer (~20 μm). The two highly porous electrodes increase the active surface area for electrochemical reactions by a factor of around 40.<sup>7</sup> The

porous geometry reduces the local current density at the Li-SE interface, which enables cycling at high current densities without any sign of dendrites. Thereby, the dense separator is acting as an additional barrier between the two porous layers since the very dense structure has a high mechanical stability and only few GBs favoring dendrite formation.<sup>7-9,29</sup>

Optimization of the porous layers will allow even further improvement of the CCD of the trilayer design. Still, the influence of the SE microstructure and GBs on lithium transport within the porous electrode is not fully understood. Electrochemical impedance spectroscopy (EIS) measurements demonstrate that GBs have a significant impact on the transport of lithium ions in the SE microstructure and become even more important in porous 3D networks.<sup>7,30,31</sup> Especially, quantitative analysis on the effect of structural bottlenecks and pinpoints on the local current density is needed in order to predict critical operation conditions causing the formation of dendrites. The transport limitation due to present GBs, which might have a detrimental influence on the ionic conductivity of the porous layer as well as the structural integrity.

Therefore, microstructure resolved continuum simulations have become an efficient tool for a detailed structural and electrochemical analysis of batteries and battery materials.<sup>32,33</sup> Simulations are performed directly on virtual microstructures of electrodes and cells and inherently include structural features of the materials.<sup>30,34-36</sup> Microstructures are typically reconstructed based on image data originating from structural characterization techniques like focused ion beam scanning electron microscope (FIB-SEM) or X-ray tomography. In our recent studies, we extend this method to microstructure resolved electrochemical simulations of ASSBs.<sup>14,37</sup> By combining electrochemical characterization of the materials with simulation studies on a digital twin, we were able to identify limiting processes for the battery performance.

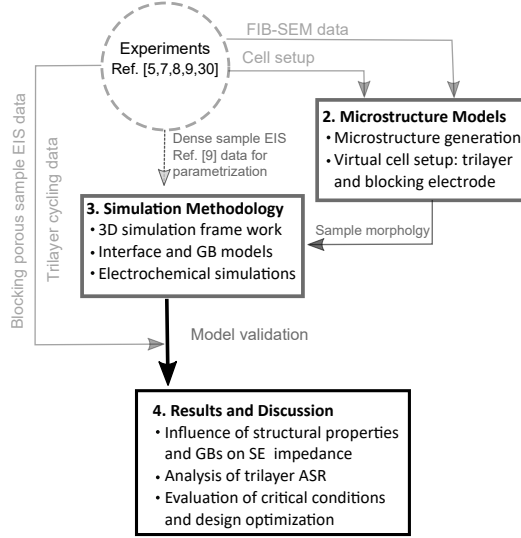


Figure 1: Schematic overview of the work flow and corresponding sections in the manuscript. Details on experimental data is given in Ref. <sup>5,7-9,30</sup>

In this study, we apply our methodology to investigate transport phenomena in porous LLZCNO samples, which is a promising component for future ASSBs. Figure 1 gives an overview of the workflow and corresponding sections in the manuscript. To validate of our model simulation, we use various experimental measurements for different cell setups on LLZCNO and metallic lithium. Thereby, we use focus on three LLZCNO samples with different porosity and grain size, which are characterized structurally and electrochemically using FIB-SEM tomography and electrochemical impedance spectroscopy (EIS),<sup>30</sup> respectively. In Section 2, the simulation setups are introduced, which are based on the segmented 3D reconstructions of the porous samples. The different virtual sample reconstructions account for the changing cell setup morphology and, therefore, are the basis for the microstructure resolved simulation studies. In Section 3, we introduce our general simulation framework including the interface models. The modified transport model also accounts for the lithium transport across GBs within the polycrystalline garnet SE. Finally, in Section 4, we discuss results of the systematic parameter studies on the two virtual cell setups and compare them against the experimental data. The validation of the impedance results allows us to assign features in the impedance spectra originating from structural properties, such as grain size, electrode

porosity, and secondary phase formation. Furthermore, we investigate lithium stripping and plating in trilayer cells using different setups and configurations. The simulations provide local information on the CCD and allow us to deduce guidelines for optimized cell designs.

## 2 Microstructure Models

In the following, we present our algorithm for the generation of virtual structures. The virtual structures are reconstructed based on data measured by FIB-SEM tomography. Details on the measurements can be found in Ref.<sup>30</sup> and in the supplementary information S1. We will focus on the image processing toolchain, which is used to segment the original grayscale data into microstructures consisting of individual grains. This segmentation enables the definition of interfaces between grains at which the modified grain boundary interface flux can be applied in the later electrochemical simulations (cf. Section 3.2.2). Furthermore, we present the different virtual cell setups which are used throughout the study.

### 2.1 Microstructure Generation

For this work, we reconstructed three different SE samples with varying porosity. An overview of the samples is given in Tabel S2, and details on sample preparation can be found in the supplementary information S1 and S2. Starting with a stack of grayscale images recorded by FIB-SEM we reconstruct 3D volume images of the samples in GeoDict.<sup>38</sup> Binarization of the images is done by setting a threshold for the grayscale value. For the analysis of secondary phases, an additional grayscale threshold is set to distinguish the third phase. The binarized volume images are then processed in MATLAB, and we perform a watershed transformation on the continuous volume image to segment the electrode and identify individual grains.<sup>39</sup> Figure 2(a) shows a representative microstructure of the highly porous sample after segmentation, where the different colors represent individual grains in-

roduced through the segmentation routine. At each interface between two adjacent grains with different color, we define the grain boundary interface flux introduced in Section 3.2.2. Despite the different colors, all grains do have the same physical and chemical properties. In the last processing step, we rescale the electrode volume to a resolution of  $0.5 \mu\text{m}$  to reduce the computational cost. The complete image processing routine is described in detail in the supplementary information S1.

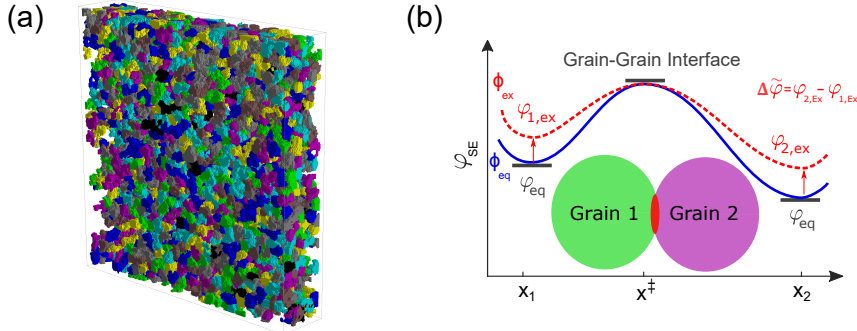


Figure 2: (a) Exemplary grain resolved microstructure obtained via the image processing routine. Connected grains with different colors define a homogeneous grain-grain interface and allow for the application of the grain flux model. The color code is used as a guide for the eye and despite the different colors, all grains do have the same physical and chemical properties. (b) First-order approximation of the electrochemical potential distribution between intersecting grains in equilibrium (solid blue) and excitation (dotted red). The fixed transition state between two grains defines the transport barrier induced by the unresolved grain boundary.

## 2.2 Impedance Setup

In the experiments, the impedance spectra of the porous samples are measured under blocking conditions. Thin gold films are deposited on both sides of the porous layers and serve as a contact to the current collectors. Details of the setup are also given Ref.<sup>30</sup> In our simulations, we reproduce the experimental setup in order to provide comparable results.

First, we create virtual samples of the porous layers characterized by EIS measurements under blocking conditions. The basis for the virtual samples are the three segmented microstructures with 56 %, 42 %, and 25 % porosity, respectively. Since we could not fully

resolve the evidence for a secondary phase formation using XRD,<sup>30</sup> we do not take them into account in our base model. The effect of virtual distributions of a secondary phase is investigated in Section 4.2.

To achieve the same thickness ( $x$ -direction) of the virtual and experimentally characterized samples, we repeatedly mirror the segmented microstructures. Through the repetition process, we preserve the specific porosities, such as grain sizes and electrode tortuosity of the original reconstructed SE volumes. All three virtual samples are cropped to identical lateral dimensions ( $y,z$ -directions) of  $100 \times 100$  voxel.

The gold electrodes are introduced as a continuous layer covering both sides of the porous SE electrode with a fixed thickness of 8 voxels. An exemplary virtual structure for the impedance simulation reproducing the experimental configuration is given in the supplementary information Figure S3. The relevant geometric parameters of the cells are listed in Table S1 and S2.

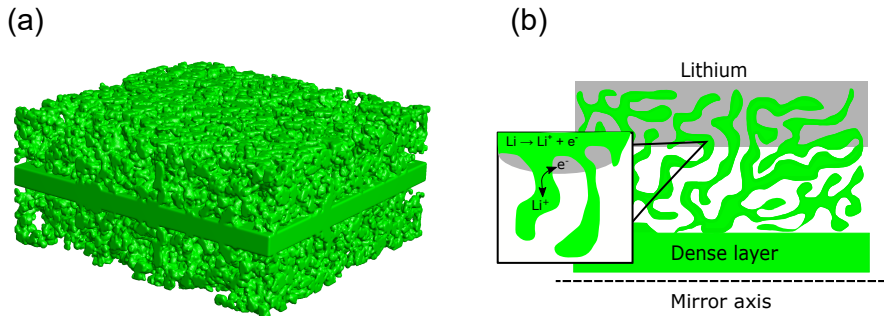


Figure 3: (a) Exemplary trilayer microstructure used for the electrochemical simulations. The grain segmentation of the porous structure was omitted for a clearer representation. (b) Schematic for a sliced trilayer framework with lithium infiltration close to the current collector. Inset: lithium reaction mechanism for the transition from the metallic into the SE phase.

### 2.3 Trilayer Setup

In ASSBs, the porous layers serve as a host matrix for the active material. Therefore, we investigate the lithium transport and cycling performance of a symmetric trilayer structure. A

schematic of this setup, which was also investigated experimentally in our previous work<sup>7,8,40</sup> is shown in Figure 3(a). For our simulations, we select the virtual sample with 56 % porosity, enabling a high energy density that is needed to outperform Li-Ion batteries with liquid electrolytes.<sup>7,41</sup> The trilayer setup consists of two porous SE layers ( $L_x = 100 \mu\text{m}$ ) separated by a dense layer of  $L_{x,\text{Dens}} = 20 \mu\text{m}$  thickness. The dimensions of the full trilayer structure are  $440 \times 100 \times 100$  voxels, which creates a virtual sample volume of  $220 \times 50 \times 50 \mu\text{m}^3$ . The dense layer is assumed to be a homogeneous layer containing no grains and GBs, as indicated by experimental measurements.<sup>7,8</sup>

In our simulations, we study the effect of lithium distribution on the area-specific resistance (ASR) and critical current density. For the different cases, the SE pore space is virtually infiltrated with lithium to reproduce different lithiation scenarios resulting from ideal plating and stripping. A schematic of the infiltrated structure is shown in Figure 3(b). If the stripping is not ideal, islands of lithium will remain on the SE surface. Therefore, we additionally mimic different lithium morphology with varying surface coverage, as discussed in Section 4.4.

### 3 Simulation Methodology

In the following section, we describe our general simulation framework for microstructure resolved electrochemical simulations. Additionally, interface models are introduced, representing both heterogeneous interfaces between SE and AM and the homogeneous interfaces, such as grain boundaries, between individual SE grains. All relevant model parameters, variables and constant with the respective description and units can be found in the supplementary information Table S4.

### 3.1 Modeling Framework

The simulation results presented in this study are based on the microstructure resolved simulation framework BEST (Battery and Electrochemistry Simulation Tool).<sup>42</sup> The dynamic evolution of the concentration, potential, and temperature distribution in the simulated cell is described by a set of coupled partial differential equations resulting from the conservation equations for mass, charge, momentum, and energy. The consistent derivation of this coupled set of partial differential equations is based on the fundamental principles of non-equilibrium thermodynamics.<sup>32</sup> A short overview of our model equations and the simulation methodology for the calculation of electrochemical impedance spectra is provided in Ref.<sup>34</sup> A prominent feature of our simulation framework is the ability to perform microstructure resolved simulations on virtual electrodes consisting of a voxel-based 3D image.<sup>35</sup> Microstructural effects, like particle morphologies or the AM and SE tortuosity, are intrinsically included. We continuously improve and extend the simulation framework to describe additional interface and transport phenomena in solid-state battery cells.<sup>14,37</sup> A summary of all transport equations for isothermal simulations can be found in the supplementary information S3.

The resolution of our 3D microstructure resolved simulations is typically lower than the width of charge imbalances, so-called space-charge layers (SCL). Therefore, we only implicitly take into account the effect of SCLs in our simulation by the corresponding interface models at GBs and with active materials described below. A detailed analysis of lithium-ion transport phenomena and interfacial processes, including SCLs on a nanometer scale within inorganic SEs, can be found in Ref.<sup>33</sup>

## 3.2 Interface Models

### 3.2.1 Active Material

At the interface between AM and SE, we assume Faradaic as well as capacitive contributions to the overall local current density. A detailed description of this approach can be found in Ref.<sup>34</sup>

The **charge transfer reaction** at the interface with Li metal (AM) is described by a thermodynamically consistent Butler-Volmer (BV) type model.<sup>43</sup> The equation for the Faradaic current is given by

$$i_{\text{BV}} = i_{00}c_{\text{SE}}^{\alpha} \left[ \exp\left(\frac{\alpha\Delta\varphi}{RT}\right) - \exp\left(\frac{-(1-\alpha)\Delta\varphi}{RT}\right) \right], \quad (1)$$

where  $i_{00}$  is the exchange current density,  $c_{\text{SE}}$  the lithium concentration in the SE and  $\alpha$  defines the symmetry factor. The driving force for the electrochemical reaction  $\Delta\varphi$  is defined by the difference in the electrochemical potential  $\varphi_{\text{SE}/\text{AM}}$  between the solid electrolyte and active materials

$$\Delta\varphi = \varphi_{\text{AM}} - \varphi_{\text{SE}} = F\Phi_{\text{AM}} - (\varphi_{\text{SE}} - \mu_{\text{Li}}) - FU_0. \quad (2)$$

The electrochemical potential difference can be reformulated by using the electrostatic potential in the active material  $\Phi_{\text{AM}}$  and the open circuit voltage  $U_0$ , with  $\mu_{\text{Li}}$  being the electrochemical potential of the lithium reference.<sup>43</sup> Note, that the electrochemical potential is given by  $\varphi_i = \mu_i + F\Phi_i$  ( $i \in \{\text{SE}, \text{AM}, G_j\}$ ) and the resulting Butler-Volmer expression is similar to the derived definition of Ref.<sup>43</sup> The detailed description of the electrochemical potential in the SE is given in the supplementary information S3 and S4.

The contact between two materials with different electrochemical potential induces the **formation of SCLs** at the interface. In liquid electrolytes this layer, consistent of two SCL on each side of the contact interface, is typically referred to as electric double layer (DL).<sup>33</sup> The thickness of the SCL in SEs is around an order of magnitude larger than in liquid sys-

tems due to the higher polarizability of the material, the crystal structure, and the reduced charge mobility.<sup>33,44</sup> In our model we do not resolve the thickness of the SCL and we use the analogy to a simple parallel-plate capacitor to account for the capacitive contributions to the interface current. Thereby, the SCL current  $i_{\text{DL}}$  assuming constant differential area capacity  $C_{\text{DL}}$  is given by

$$i_{\text{DL}} = C_{\text{DL}} \frac{d(\Delta\Phi)}{dt}. \quad (3)$$

The electric potential difference  $\Delta\Phi$  between the AM and SE across the SCL can be calculated according to

$$\Delta\Phi = \Phi_{\text{AM}} - \Phi_{\text{SE}}. \quad (4)$$

Further details are given in the supplementary information S3 and Ref.<sup>34</sup> In our interface model we assume that the Faradaic current Equation (1) and SCL current Equation (3) are in parallel. The sum of both contributions accounts for the **exchange of mass and charge** at the interface between AM and SE

$$\vec{N}_{\text{AM}} \cdot \vec{n}_{\text{A}} = N_{\text{BV}}, \quad (5)$$

$$\vec{J}_{\text{AM}} \cdot \vec{n}_{\text{A}} = i_{\text{BV}} + i_{\text{DL}}, \quad (6)$$

$$\vec{N}_{\text{SE}} \cdot \vec{n}_{\text{A}} = N_{\text{BV}} + N_{\text{DL}}, \quad (7)$$

$$\vec{J}_{\text{SE}} \cdot \vec{n}_{\text{A}} = i_{\text{BV}} + i_{\text{DL}}. \quad (8)$$

Thereby,  $\vec{N}_{\text{AM}}$  and  $\vec{N}_{\text{SE}}$  denote the molar flux densities and  $N_{\text{BV}}$  and  $N_{\text{DL}}$  are the corresponding molar interface fluxes along the surface normal vector ( $\vec{n}_{\text{A}}$ ) of lithium given by  $i_{\text{BV}}/F$  and  $i_{\text{DL}}/F$ , respectively.  $F$  denotes the Faraday constant. We emphasize that this approach is generic, and different expressions for the Faradaic and SCL current can be introduced to improve the level of detail and model predictions.

### 3.2.2 Grain Boundaries

For the interface flux between two SE grains, we additionally need an interface model which describes the transport of lithium across the grain boundary, as well as takes into account the SCLs due to misorientations of the crystal lattices.<sup>25,45,46</sup>

At a grain boundary, two grains with different crystalline orientations are in contact, which presents a transport barrier for the flux of lithium ions. Furthermore, amorphous interphases<sup>47,48</sup> may form at GBs, which presumably enhance the transport barrier and therefore electrochemical potential step height. In a first approach, we model the transport of lithium across the GB by a hopping process, which is derived in the transition state theory<sup>43,49</sup> and results in a Butler Volmer-like expression.

The electrochemical potential distribution at equilibrium and after excitation ( $\varphi_{i,\text{Ex}}$ ) through an external potential is schematically shown in Figure 2(b). As a first approximation, we assume that the electrochemical potential of the transition state at the GB is only a function of temperature and the rate of lithium transfer is given by a hopping rate  $k_{\text{hop}}$ . In this case the interface current between two adjacent grains  $G_i$  and  $G_j$  is described by

$$i_{\text{GB}} = k_{\text{hop}} \sqrt{\tilde{c}_{G_i} \tilde{c}_{G_j}} \left[ \exp\left(\frac{\Delta\tilde{\varphi}}{2RT}\right) - \exp\left(\frac{-\Delta\tilde{\varphi}}{2RT}\right) \right] \quad (9)$$

Since under isothermal conditions the electrochemical potential of the transition state is constant also the hopping rate is fixed. A brief derivation of the resulting GB current expression is given in the supplementary information S4. The driving force for the lithium transfer reaction is given by the modified electrochemical potential difference  $\Delta\tilde{\varphi} = \varphi_{G_i} - \varphi_{G_j}$ , which is defined as the difference in the bulk electrochemical potentials of the two adjacent grains (subscripts  $\{j, i\}$ ) separated by the GB interface, as shown in Figure 2(b).

As experimentally shown,<sup>25,45,46</sup> the electrochemical potential step along the GB, due to misalignment of the crystal lattice and additional material changes in the GB, facilitates the formation of screening charges (SCLs) in its vicinity. Since we do not spatially resolve

the GB or electrochemical gradients along the SCLs, we adapt the model approximation for capacitive contributions as introduced above. The modified double layer model from Equation 3 enables us to incorporate the effective SCL formation at the GB and accounts for the resulting polarization process. Therefore, we obtain similar expressions for the exchange of mass and charge across the grain boundary given by

$$\vec{N}_{\text{SE},G_i} \cdot \vec{n}_A = N_{\text{GB}} + N_{\text{DL}}, \quad (10)$$

$$\vec{J}_{\text{SE},G_i} \cdot \vec{n}_A = i_{\text{GB}} + i_{\text{DL}}. \quad (11)$$

The definitions of the molar fluxes corresponds to Equation 5-8. Note that this interface model is a first step to take into account the effect of GBs and SCLs in polycrystalline SEs. In our future work, we aim at multi-scale simulations for the description of interface fluxes and SCLs. Enabling us to include our derived theory-based input parameters, e.g., for the hopping rate or SCL capacity, accounting for the potential and concentration distribution within the grain boundary.

**Secondary Phase** The secondary phase is assumed to be an isolating material phase and block the lithium transport to the SE. Therefore, the mass and charge transfer  $N_{\text{GB}}$  and  $i_{\text{GB}}$  is omitted for the interface expression. Nevertheless, to account for the additional interface charging through the non-vanishing permittivity of the secondary phase, we preserve the DL interface condition for our model.

### 3.3 Model Parametrization

In the following section, we introduce bulk transport parameters and parameters of the interface models used in our simulations. All relevant simulation parameters and operation conditions are summarized in the supplementary information S5.

**Bulk Transport** The composition and density of LLCZNO were determined in previous works.<sup>7,9</sup> This corresponds to an average lithium concentration of  $c_{\text{Li}}^{\text{SE},0} = 0.0384 \text{ mol/cm}^3$ . Bulk transport parameters of LLCZNO for our simulations are either extracted from literature or are measured by the authors. The most decisive transport parameter is the ionic conductivity of the SE. We estimated the bulk ionic conductivity within the grains  $\sigma_{\text{Li}}^{\text{SE}} = 7.69 \times 10^{-4} \text{ S/cm}$  using EIS measurements on highly dense LLCZNO pellets.<sup>9</sup> This is also in line with previous measurements published in the literature, which range from  $2.4\text{--}7.69 \times 10^{-4} \text{ S/cm}$  at room temperature.<sup>7-9,30</sup> The secondary phase is assumed to be SE type phase with a reduced ionic conductivity by orders of magnitude compared to the regular SE. The conductivity is set to  $\sigma_{\text{Li}}^{\text{SE}} = 1.0 \times 10^{-9} \text{ S/cm}$ , which can be regarded as isolating for the ionic transport.<sup>30</sup>

The Li-ion diffusion coefficient  $D_{\text{Li}}^{\text{SE}} = 5.36 \times 10^{-9} \text{ cm}^2/\text{s}$  is calculated from these measured lithium ion conductivities based on the assumption of negligible interactions between lithium ions and lattice vacancies using  $D_{\text{Li}}^{\text{SE}} = \sigma_{\text{SE}} RT / c_{\text{Li}}^{\text{SE},0} F^2$  with  $T$  the absolute temperature,  $F$  the Faraday constant, and  $R$  the gas constant. LLCZNO is generally regarded as a single ion conductor with negligible electric conductivity. Therefore, we set the transference number of lithium ions to  $t_{\text{Li}}^+ = 1$ .

In our simulations, the electronic pathways in the porous layers are either through the metallic lithium phase or electronically conductive surface coatings. We use an electronic conductivity of lithium metal of  $\kappa_{\text{Li}}^{\text{AM}} = 10 \times 10^4 \text{ S/cm}$ , which is orders of magnitude higher compared to the lithium-ion conductivity of the SE and therefore can be seen as an ideal conductor. Since we do not explicitly simulate the lithium stripping and plating and rather investigate the current distribution via potential initialization, the lithium-ion concentration is assumed to be an infinite reservoir of charge carriers.

**Lithium Interface** Recent work on garnet-type materials has shown that the interface resistance between lithium and the garnet is dominated by the surface roughness and the wetting behavior of lithium metal. By increasing the cell pressure up to 400 MPa during cycling, the induced plastic flow of lithium metal increases the contact and leads to a negligible charge transfer resistance.<sup>17</sup> A comparable, and more easily scalable, effect on the interface resistance was achieved by ALD coating of 5 nm alumina on the garnet SE. The coating improved the wetting behavior of lithium metal and reduced the interface resistance down to a similar negligible interfacial impedance of only  $1 \Omega\text{cm}^2$ .<sup>9</sup> In addition, the alumina coating is expected to prevent potential interface degradation and interlayer formation at the lithium interface as observed for uncoated garnets.<sup>50,51</sup> Various functional coatings for LLCZNO have been demonstrated, such as alumina,<sup>7,9</sup> zinc oxide,<sup>52</sup> aluminum<sup>29</sup> and germanium<sup>53</sup> to improve the interface wetting between lithium metal and the SE. The coating film thickness is in the nanometer range and, therefore, cannot be explicitly resolved in our cell-level simulation. The aspect of interface modifications through coatings is taken into account by selecting the corresponding parameters for interface reactions. In the trilayer simulations we use an exchange current density factor  $i_{00}^{\text{Li}} = 2.59 \times 10^{-2} \text{ A/cm}^2$  for the AM|SE interface reaction measured by Han *et al.* using EIS on dense LLCZNO samples in a symmetric cell setup.<sup>9</sup>

**Blocking Electrodes** For the cell configuration with blocking gold electrodes, the exchange current density  $i_{00}^{\text{Au}}$  was reduced to  $1 \times 10^{-8} \text{ A/cm}^2$  to suppress the charge transfer reaction at the interface. The DL capacity of the gold electrode was adjusted to  $C_{\text{DL}}^{\text{Au}} = 2.4 \times 10^{-4} \text{ F/cm}^2$  based on the experimental data to reproduce the experimental impedance response at low frequencies.

**Secondary Phases** To suppress the lithium transfer between the secondary phase and the SE, the exchange current density  $i_{00}^{\text{SP}}$  is set to  $1 \times 10^{-8} \text{ A/cm}^2$ . For a first approximation the double layer capacity is fixed at  $C_{\text{DL}}^{\text{SP}} = 1 \times 10^{-6} \text{ F/cm}^2$ , since the experimental EIS

measurements indicate a presumably occurrence in the mid-frequency range ( $10^5$ - $10^2$  Hz). A detail discussion on the transport and structural influences on the resulting impedance response is given in Section 4.2.

**Grain Boundaries** For the parametrization of the homogeneous SE interface reaction, we use EIS measurements on dense pellets published in Ref.<sup>9</sup> These measurements are used to estimate the hopping rate  $k_{\text{hop}}$  and the DL capacity  $C_{\text{DL}}^{\text{GB}}$  which are in a second step refined manually to improve the agreement with the experimental data. The corresponding impedance simulation of the dense virtual sample is given in the supplementary information S5. Note that we use the same set of grain boundary parameters given in Table S4 for all simulations shown in this publication.

### 3.4 Electrochemical Simulations

**Electrochemical Impedance Spectroscopy** Electrochemical impedance spectra are measured and simulated on the porous samples in the configuration described in Section 2.2. In both cases, frequencies range from 17 MHz down to 1Hz. For the simulation of impedance spectra, we use the step-excitation method outlined by Hein *et al.*,<sup>34</sup> and more details on our experiments can be found in.<sup>30</sup>

**Simulation of ASR** The ASR is an important quantity for battery development. In our simulations, we calculate the ASR for a given lithium distribution within the porous SE samples of the trilayer setup. Thereby, we investigate different morphology and surface coverage introduced in Section 2.1. We apply a constant current at the current collectors for each configuration and solve for the stationary distribution of potentials and local current densities. The data is then used to calculate the ASR and analyzed for the local current density distribution within the trilayer.

Note, that our continuum modeling framework is not able to model the time-resolved lithium

nucleation and film growth during stripping and plating in the SE structure. Nevertheless, our microstructure-resolved simulation approach enables us to resolve transport phenomena on the cell level scale, which can be again validated against experimentally accessible quantities such as the ASR and CCD. To extract these quantities from our simulation, we need to simulate specific cell configuration, which recreate experimentally observed or expected snapshots.

## 4 Results and Discussion

### 4.1 Structural Analysis

This section presents the structural analysis for the three reconstructed samples with varying porosity based on the segmented FIB-SEM volume images. The material composition, sample tortuosity, and average particle size are listed in Table 1.

Table 1: Structural parameters calculated based on segmented FIB-SEM reconstructions of the samples with varying porosity: material composition by vol-%, SE tortuosity, SE specific surface area, approximated GB specific surface area and average particle size.

parameter, unit	Sample 56	Sample 42	Sample 25
Material composition, vol-%			
Pore space	56.61	42.6	25.0
LLCZNO	42.6	55.9	75.0
Secondary phase	0.77	1.7	0
Specific surface area SE			
$A_{\text{Spec,SE}}, \times 10^4 \text{ cm}^2/\text{cm}^3$	2.18	0.93	0.66
Specific surface area GB			
$A_{\text{Spec,GB}}, \times 10^4 \text{ cm}^2/\text{cm}^3$	1.37	1.08	1.35
SE tortuosity (direc.)			
$x$	1.75	1.45	1.21
$y$	1.68	1.34	1.15
$z$	1.78	1.26	1.20
Average particle diameter, $\mu\text{m}$			
$d$	3.1	4.59	4.62

The three analyzed samples show a varying porosity of 56.6, 42.6, and 25.0 vol-% and a LLCZNO volume fraction of 42.6, 55.9, and 75.0, respectively. These values are in line with

the composition estimated based on the density of the samples. The electrode surface area shows the expected trend with decreasing pore space volume. Additionally, we find in our reconstructions artifacts in the samples with higher porosity which might point to secondary phase formation. Reports of degradation and secondary phases due to anion migration in the lattice or lithium evaporation during sintering can be found, for instance, in Ref.<sup>54–56</sup> However, in our previous work<sup>30</sup> we could not identify the chemical composition of these artefacts due to the relatively low quantity. A simulation study shedding some more light on this issue can be found in Section 4.2.

The tortuosity of the transport pathways within the SE structure determines the ohmic resistance of the porous layers. All three samples show an increase in tortuosity with increasing porosity of around 44 %. In our analysis, we do not observe significant deviations between tortuosity values in the three spatial directions, which implicates a rather isotropic and homogeneous SE structure. The rise in tortuosity with increasing porosity prolongs the pathways for lithium transport and, therefore, increases the ionic resistance of the porous SE layer. This result is in agreement with the structural analysis in our previous work<sup>30</sup> the simulated effective conductivities discussed in Section 4.3.

Moreover, we use the segmented reconstruction to estimate the particle size distribution. Details on the calculation are given in the supplementary information S1.1 and S1.2. The resulting average particle sizes for all three samples are listed in Table 1. The comparison shows that the average particle size for the highest porosity ( $d_{56} = 3.1 \mu\text{m}$ ) is around 32 % smaller than for the two samples with lower porosity where the diameter is around  $4.6 \mu\text{m}$ . The reduced particle size increases the effective SE surface area (cf. Table 1) and, therefore, potentially leads to enhanced surface degradation during sintering. The reconstructions do not allow to deduce a clear trend for the formation of secondary phases (cf. Table 1). However, the impedance simulations presented in Section 4.2 indicate that the impedance spectra of samples with high porosity show a pronounced additional feature which could be linked to the formation of a secondary phase.

The specific surface area for the SE phase, as well as the specific GB surface area, are also listed in Table 1. We can clearly see the aforementioned rise in the specific surface area between the SE and the pore space for increasing porosity. For the porous SE layer design, the high specific surface area might present one strategy to mitigate dendrite formation in high power applications, since a larger SE surface area decreases the local current densities. A detailed analysis of this effect is presented in Section 4.4. Moreover, we observe a slight increase in the GB interface area with growing porosity. Even though the samples with 56 % and the 25 % porosity have comparable specific GB surface area, due to longer lithium transport pathways, the highly porous sample is expected to show higher GB contributions to the overall impedance (cf. Section 4.2).

## 4.2 Impedance Analysis

In the following section, we analyze the impedance spectra of the different SE samples. Our model is parameterized using a dense sample, and in this section, we apply it to the simulation of electrochemical impedance spectra of the reconstructed virtual samples with different porosity. Furthermore, we investigate the effect of secondary phases on the impedance and compare our simulations to conductivity measurements.

**Bulk and Grain Boundary Processes** Following the structural analysis, we begin the discussion of the electrochemical simulations with an impedance analysis of the porous SE sample with 25 % porosity. The schematic of the blocking electrode configuration used for the shown impedance study is given in the supplementary information S2. Thereby, we focus on a general discussion and comparison of simulated and experimental impedance spectra. In our analysis, we assign features in the impedance spectra to physical and chemical processes described in our model and evaluate the effect of grain boundaries.

Even within our model framework, the assignment of processes is challenging, since mi-

nor changes in the material composition significantly change the EIS response. Several impedance studies on LLCZNO materials are published in the literature,<sup>9,30,57</sup> each of them providing a different interpretation of the data. In these cases, the impedance analysis is based on a fit of equivalent circuit models to the measured impedance spectra. In contrast, impedance simulations presented in this study are based on our continuum model, describing the most relevant physico-chemical processes in the cell. Parameters are determined using impedance and conductivity data of a dense sample,<sup>9,29</sup> and the corresponding simulation results can be found in the supplementary information S5. Additionally, we perform simulation studies in order to evaluate the effect of changes in bulk conductivity and secondary phases in the following paragraphs.

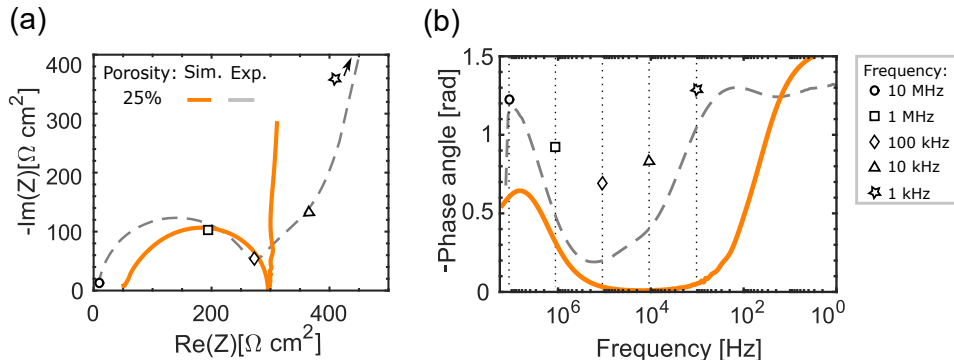


Figure 4: (a) Nyquist plot representation of the impedance response and (b) phase angle evolution in frequency space for the sample with 25 % porosity: simulated (orange) and experiment (dotted gray). The open symbols mark the corresponding frequencies in the experimental data.

Figure 4(a) shows the impedance spectra of the SE sample with 25 % porosity, and thickness of 217  $\mu\text{m}$ . The simulation results are shown as a solid orange line, and the dashed gray line gives the experimental data. The corresponding phase angle diagram in the frequency space is shown in Figure 4(b). The full Bode plot of the impedance data is given in the supplementary information S10.

In the experimental data, we observe a distinct feature in the high-frequency regime above  $10^6$  Hz. In the mid-frequency regime, around  $10^5$ - $10^3$  Hz, a second process emerges, which

overlaps with the high-frequency process in the Nyquist plot (cf. Figure 4(a)). At lower frequencies, we observe in the phase angle diagram another feature around  $10^1$  Hz which is commonly assigned to the impedance of the gold electrodes.<sup>29</sup>

In our model, we do not take into account the polarization of the bulk SE grains. Therefore, the intersection with the real axis at around  $53 \text{ } \Omega\text{cm}^2$  in our simulated impedance spectra includes the effective bulk resistance and the corresponding bulk polarization. The magnitude of the bulk contribution is also determined by the tortuosity in the porous SE sample, which increases the transport pathways for the ions and the effective ionic bulk resistance, respectively. This effect becomes more prominent for increasing sample porosity, as discussed in the following section.

The studied SE samples possess selective characteristic frequencies  $f_C$  where different polarization processes, such as the bulk or GB polarization, show their maximum amplitude in the impedance measurement. We estimate the expected characteristic frequency of bulk processes  $f_{C,B}$  based on the effective bulk permittivity  $\varepsilon_{\text{eff}}$  and conductivity of the porous sample. The characteristic frequency can be calculated according to  $f_{C,B} = \sigma_{\text{eff, bulk}} (2\pi\varepsilon_{\text{eff}}\varepsilon_0)^{-1}$  with  $\varepsilon_0$  being the vacuum permittivity. We approximate the effective permittivity  $\varepsilon_{\text{eff}}$  with by the Bruggeman mixing rule<sup>58</sup> (cf. supplementary information S6). In our consideration, we neglect contributions of the GB due to their small thickness and comparably small volume fraction (<7 vol-%). The LLZCNO bulk permittivity value is determined around 75.<sup>59,60</sup> Assuming that the remaining pore space is filled with air, we get an effective relative permittivity of  $\varepsilon_{\text{eff}} = 47$  for the sample with 25 % porosity. Compared to the dense sample with a bulk relative permittivity of  $\sim 75$ , this is a reduction by 37 %. The effective ionic bulk conductivity for the 25 % sample ( $\sigma_{\text{eff, bulk}} = 3.66 \times 10^{-4} \text{ S/cm}$ ) is based on our calculations given in Section 4.3. Note, that the expected bulk characteristic frequency  $f_{C,B} = 1.40 \times 10^7 \text{ Hz}$  is close to the upper-frequency limit of the measurement setup, which is around  $1.5 \times 10^7 \text{ Hz}$ . The limited resolution above  $1 \times 10^7 \text{ Hz}$  results in the steep increase of the phase angle mea-

surement shown in Figure 4(b).

The bulk processes are followed by the GB contribution in the frequency range between  $10^7$  to  $10^6$  Hz. In this frequency range, the simulated phase angle resulting from GB processes is in qualitative agreement with the experimental data. Since the bulk polarization contribution enters as a constant shift along the  $x$ -axis in our model, we therefore cannot account for the superposition of the two polarization contributions as measured in the experiment. This results in the observed misalignment in the phase angle and impedance plot for the high frequency range between simulation and experiment. In our simulations, we use a capacity for the space charge layers of  $C_{DL} = 9.75 \times 10^{-9}$  F/cm<sup>2</sup>, which is in the range reported in the literature for this type of process.<sup>61</sup> Based on the kinetic factors for the transport across the GB, we estimate a characteristic frequency for the GB polarization around  $f_{C,GB} = 7.0 \times 10^6$  Hz.

In the mid-frequency regime ( $10^5$ - $10^3$  Hz), we do not observe the additional feature seen in the experiments, which indicates that our model misses a process causing a characteristic in this frequency range. This observation might point to the secondary phase, which is not included in these simulations and will be discussed in detail in the following paragraphs.

Instead, in our simulations, the grain boundary processes are followed directly by the feature of the blocking gold electrodes in the low-frequency range. Since we assume ideally blocking behavior on a flat surface, the corresponding increase in the imaginary part is steeper than observed in the experiments.

Based on the limited number of frequency points above  $1 \times 10^7$  Hz and the observed misalignment of the first resonance in the phase angle diagram to the first semi-circle in the Nyquist plot, we assume that the bulk polarization process is not fully resolved in the experiments. Therefore, a straightforward decomposition and assignment of the bulk and GB polarization contribution in the experiments is more complex. In combination with our simulations, we conclude that we have an overlap between bulk and GB processes in the frequency regime between  $10^7$  to  $10^6$  Hz in the experimental data. Thereby, the bulk contribution is smaller

in magnitude and the contribution of the GBs dominates the impedance. This conclusion is also in agreement with measurements on dense samples (cf. supplementary information Figure S4) of LLCZNO.<sup>9,29</sup>

**Effect of Porosity** In this paragraph, we compare the predictions of our simulations on virtual samples with different porosity to impedance data measured on the actual samples. We want to emphasize that the parametrization for all three samples is identical, and therefore, changes in our simulations arise only due to differences in the sample microstructure. Changes in SE properties e.g., due to lithium loss and formation of secondary phases during sintering, will be analyzed in the paragraphs below.

In Figure 5 the measured (gray dashed lines) and simulated (solid lines) electrochemical

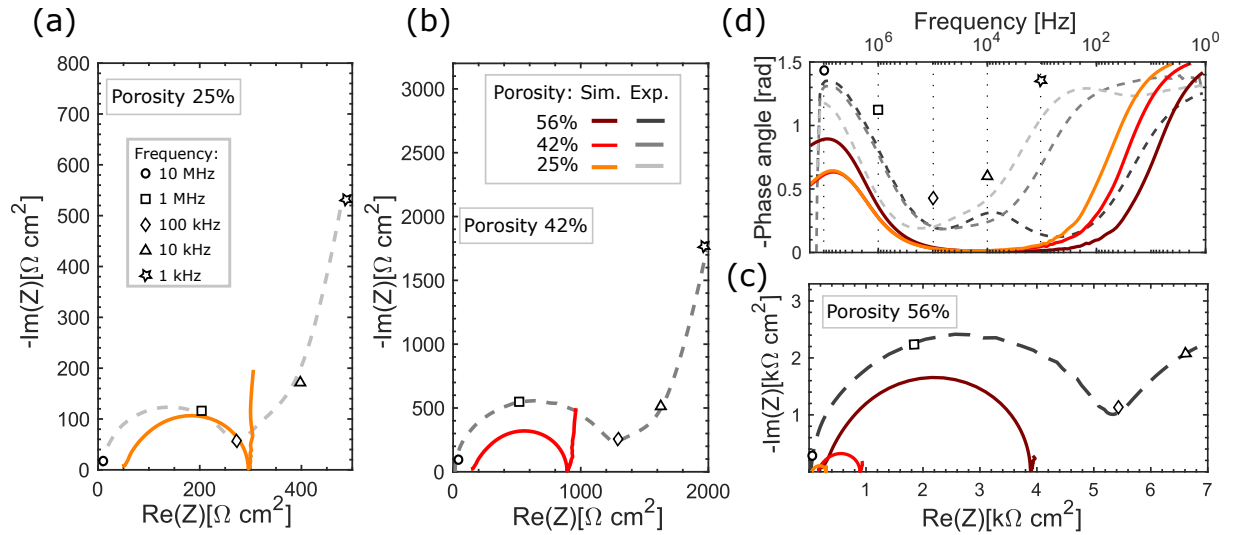


Figure 5: Nyquist plot representation and (d) phase angle evolution in frequency space for the impedance response of all reconstructed samples: 56 % (dark red), 42 % (red) and 25 % (orange) porosity. The open symbols mark the corresponding frequencies in the experimental data.

impedance spectra are shown for all three reconstructed samples with 25 %, 42 %, and 56 % porosity. Figure 5 (d) additionally presents the phase angle as function of frequency to supplement our discussion of the impedance spectra. In our measurements and simulations, we observe a substantial increase in the impedance with increasing porosity. This is in line

with the general picture that the impedance is proportional to the tortuosity of transport pathways. Moreover, we observe that with decreasing porosity, simulated impedance spectra show better agreement with the experimental data (cf. Figure 5(a) and (b)). Since we parametrized our model with impedance measurements on a dense pellet ( $\leq 2\%$  porosity), we expect and do indeed see the best agreement with the sample with low porosity discussed in the previous paragraph. With increasing porosity, deviations become significant. This indicates that additional effects in the samples with higher porosity contribute to the increase in impedance measured in the experiments. One aspect might be degradation phenomena during sintering due to the large specific surface area of the highly porous samples.<sup>30,60</sup> In the Nyquist plot for our simulations, we observe a shift of the high frequency intersection with the real axis. This corresponds to an increase in bulk resistance with porosity and tortuosity, respectively. The measurements do not show the same shift, which again points at overlapping contributions of bulk and GB processes in the high-frequency regime.

Note that the tortuosity also affects GB contributions. Although the specific GB surface area values for the 56% ( $A_{\text{Spec,GB}} = 1.37 \times 10^4 \text{ cm}^2/\text{cm}^3$ ) and 25% ( $A_{\text{Spec,GB}} = 1.35 \times 10^4 \text{ cm}^2/\text{cm}^3$ ) sample are comparable, the reduced tortuosity in the 25% sample provides shorter pathways for the lithium transport and consequently reduces the number of GBs along the path. In contrast, for the highly porous sample, the reduced grain size and larger tortuosity give rise to a higher number of grain boundaries along the lithium transport pathway. Therefore, we see higher GB resistance in our simulations for the highly porous sample and comparable to reported experimental data.<sup>15,62-64</sup> In general, we notice that our model underestimates the impedance at high frequencies by almost 30% for the highly porous samples. The deviation could be an indication for changes in bulk or GB conductivity during processing of the porous SE materials.

The EIS measurement shown in Figure 5(a) demonstrates that with increasing porosity of the SE, the process around  $10^4$  Hz becomes much more prominent. In the sample with 56%

porosity, we even observe a distinct semi-circle in our measurements, as shown in the following paragraph on secondary phases. As discussed above, this trend is proportional to the increase in specific surface area of the samples and also points to an increasing lithium loss in the highly porous samples. At some point even the tetragonal phase might be formed, which has a significantly lower ionic conductivity.<sup>56,60</sup> Moreover, the phase angle diagram displayed in Figure 5(d) indicates that the characteristic frequency of the process shifts towards lower frequencies ( $10^3$  Hz) with reducing porosity and eventually overlaps with the contribution of the gold electrode. Additionally, we suggest that through the increasing tortuosity (Table 1) of the samples, the ionic transport becomes more sensitive to phase impurities or areas with lower conductivity. Lithium ions need to cross a higher number of GBs, and the effect of secondary phases with low conductivity becomes more dominant.

Multiple studies on garnet SEs, like LLZO,<sup>54–56</sup> report lithium loss at the particle surface exposed to air during sintering, changing the composition and conductivity of the material. This change in lithium stoichiometry on the SE surface could modify the effective bulk conductivity as well as the grain boundary composition, leading to an overall reduced transport. In the following paragraph, we will first focus on the effect of decreasing bulk conductivities during sintering before turning our attention to the effect of secondary phases.

**Effect of Bulk Conductivity** The increasing deviation between impedance measurements and simulations for the highly porous samples indicates a reduction of transport parameters during sintering. Therefore, we investigate the influence of changing bulk conductivity on the impedance. Figure 6 shows Nyquist plots for the samples with 42% and 52% porosity with varying bulk conductivity. Note, that we only change the bulk conductivity  $\sigma_{\text{bulk}}$  from  $7.69 \times 10^{-4}$  S/cm down to  $2.0 \times 10^{-4}$  S/cm. We emphasize that all other model parameters are unchanged in this study.

Simulations of the sample with 42% porosity are shown in Figure 6(a), where solid lines give the simulation data, and the gray dotted lines provide the corresponding experimental

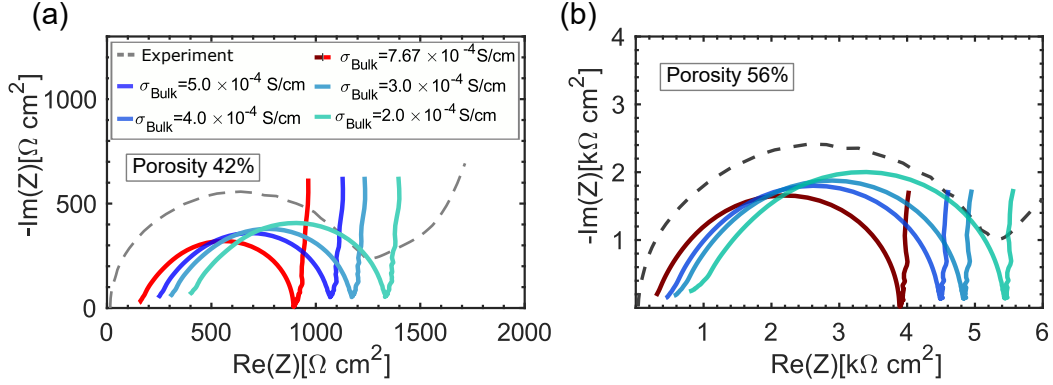


Figure 6: Nyquist plot representation of the impedance response with reduced bulk conductivity from  $7.69\text{--}2.0 \times 10^{-4}$  S/cm: (a) 42 % porosity sample and (b) 56 % porosity sample.

measurement. As expected, the decreasing bulk conductivity causes a shift along the  $x$ -axis, reflecting the increasing bulk resistance of the sample. Thereby, the simulated spectra with a bulk conductivity of  $3.0 \times 10^{-4}$  S/cm (light blue) shows the best agreement with the experimental data. The same trend is also seen for the sample with 56 % porosity displayed in Figure 6(b). There we see the best agreement with the experimental data at slightly lower bulk conductivity around  $2.0 \times 10^{-4}$  S/cm (cyan). Therefore, we see a reduction in bulk conductivity by 60 % and 75 % for the samples with 42 %, and the 56 % porosity, respectively. Moreover, we can observe that also the semi-circle linked to the GB contribution increases with decreasing conductivity. Again, the rise in GB contribution is more pronounced for the highly porous sample due to the higher tortuosity and larger specific GB surface area.

Therefore, we conclude that a reduction of conductivity due to lithium evaporation at exposed SE surfaces could be one reason for the increase in impedance with SE porosity.

Even though the lithium loss is occurring predominantly at the SE surface, we assume that evaporation in the proximity of grain boundaries could as well result in a change of the GB composition. A similar study on the GB transfer resistance contribution can be found in the supplementary information S7. The GB resistivity study emphasizes the strong dependence of the impedance response on the GB transport parameter. The increase of the GB charge transfer resistance by 25 % improves the agreement between simulation and experiment,

similar to the effect of the bulk conductivity. Since both degradation mechanisms possess a similar effect on the impedance response, an exact deconvolution of both contributions via EIS is unfeasible without additional information on the GB composition.

Nevertheless, the change in bulk and GB conductivity do not reproduce the second semi-circle in the mid-frequency regime. Therefore, we will investigate the effect of secondary phases on the impedance spectra in the next paragraph.

**Effect of Secondary Phases** Generally, the analysis in the previous paragraphs indicates that the mid-frequency polarization process becomes more distinct with increasing porosity. Especially for the sample with 56 % porosity the polarization contribution in the mid-frequency regime becomes clearly distinguishable, as shown in Figure 7(b)(gray curve). We assume that the mid-frequency polarization contribution is related to the formation of a secondary phase, which is promoted by the rising sample porosity and the amplified lithium loss. This assumption was supported by FIB-SEM images, which indicate the formation of such a secondary phase in the sample. Therefore, we proceed to investigate the influence of this aspect in more detail. Since the observed features in the impedance data cannot be uniquely assigned to secondary phase formation, we acknowledge that further effects, such as the formation of interlayers at the SE| metal interface<sup>50,51</sup> or additional surface diffusion effects in the garnet structure could be related to the mid-frequency processes. Nevertheless, our experiments do not provide a clear indication on the aforementioned phenomena and we therefore focus on the structural aspects of the secondary phase formation and distribution.

Starting point are the SEM images of the highly porous sample, which show features of a secondary phase indicated by a difference in gray-scale value. An exemplary image for the spatial distribution of the secondary phase is given in the supplementary information S1.3. However, in the highly porous sample, the content is as low as 0.77 vol-%, and contributions of measurement artifacts can not be excluded. Moreover, no additional phases were found

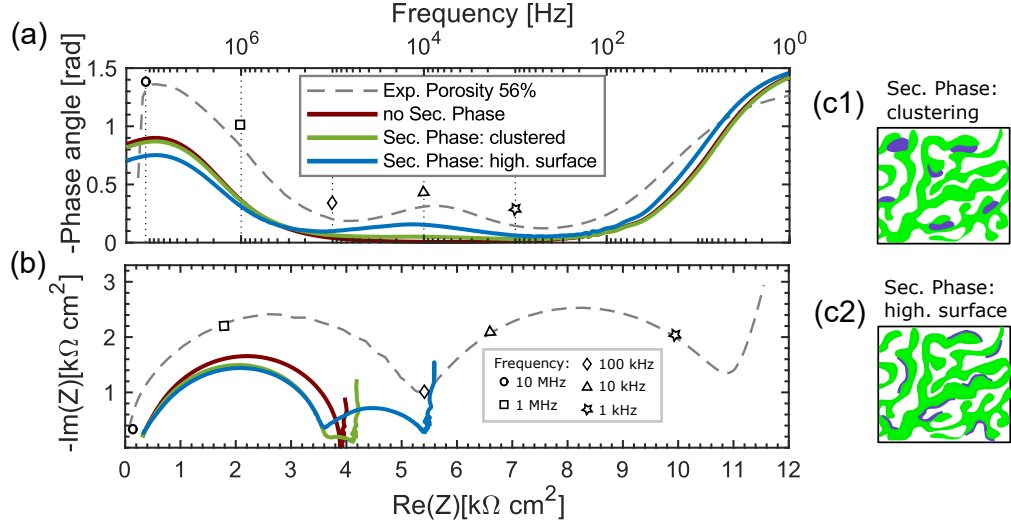


Figure 7: (a) Phase angle evolution against frequency and (b) Nyquist plot representation of the impedance response for varying secondary phase distribution: no secondary material (red), clustering (green), reduced clustering/increased surface coverage (blue). (c) Schematic representation of the secondary phase distribution in the porous sample. The open symbols mark the corresponding frequencies in the experimental data.

in XRD measurements since such small amounts are below the detection limit.

Still, secondary phases or phase impurities such as the tetragonal phase are also reported in the literature.<sup>54,56</sup> Therefore, we perform a simulation study on the effect of secondary phases. We expect that this phase is poorly conductive,<sup>30</sup> yet polarizable. The corresponding parameters are given in Section 3.1.

Figure 7 shows simulated impedance spectra for the sample with 56% porosity and varying secondary phase distribution. The corresponding phase angle diagram in the frequency space is shown in Figure 7(a). The solid green line in Figure 7(b) shows the impedance response for the unmodified secondary phase distribution as reconstructed from FIB-SEM. As shown in the upper schematic Figure 7(c1), the secondary phase seems to form small clusters in the SE pore space at bottlenecks between SE grains. Based on the FIB-SEM reconstruction, we estimate that  $\sim 1.2\%$  of the SE surface is in contact with the secondary phase. As indicated in the phase angle diagram in Figure 7(a), the inclusion of the secondary phase causes a small feature in the mid-frequency range around  $5 \times 10^3$  Hz. Due to the low volume and contact area to the SE, the resulting contribution in the Nyquist plot is small relative to the

first semi-circle. Still, it is an indication that even small amounts of phase impurities can cause the second feature seen in the experiments.

Thin surface films of secondary phases forming due to lithium evaporation at the SE surface might be challenging to resolve in the SEM. In order to shed some more light on this topic, we artificially distribute a thin layer of a non-conductive phase on the SE surface (cf. Figure 7 (c2)). The resulting surface coverage of this approach is still as low as  $\sim 2.2\%$ . The corresponding simulated impedance spectra are shown as solid blue lines in Figure 7.

The redistribution of the thin film with a higher surface area increases the contribution of the secondary phase significantly, resulting in a distinct semi-circle. Although the impedance is still smaller than in the experimental data, the qualitative trends in the Nyquist plot (Figure 7(b)) and phase angle (Figure 7(a)) show better agreement.

As discussed in the previous paragraphs, the changing bulk and grain boundary transport properties due to degradation during sintering, could be the origin of the deviation between experiments and simulations. Again, we want to emphasize that we do use the same set of parameters in our simulations. Therefore, we expect that our model simulations only reproduce qualitative trends observed in the experiments.

Nevertheless, based on the results presented in this study, we conclude that a thin polarizable layer of a secondary phase could be forming on the surface of the porous sample during sintering. As indicated by the analysis presented in Ref.,<sup>30</sup> this thin secondary phase film will be most likely hard to distinguish in the FIB-SEM images and below the detection limit of the XRD.<sup>30</sup> Since our simulated distribution is artificial, we can only draw qualitative conclusions on the phase formation and its influence. Further analysis is necessary to determine morphological and structural properties.

### 4.3 Effective Conductivity

In the next step, we will use our parametrized model for the porous SE sample to estimate the effective ionic conductivity taking into account both the effect of the microstructure and grain boundaries. Figure 8 shows the effective ionic conductivity of the samples with

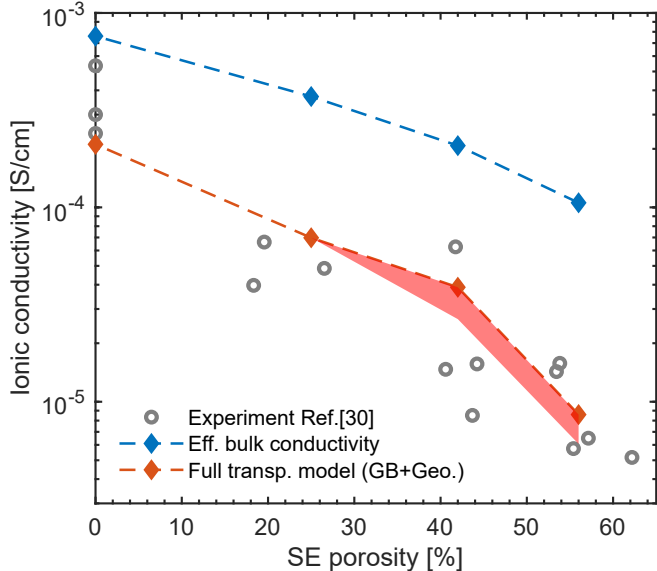


Figure 8: Experimental ionic conductivity (gray symbols) taken from Ref.<sup>30</sup> and calculated ionic conductivity of the different electrode samples for varying model conditions: structural model (dotted blue) and fully model combining structural and grain boundary transport (solid red). The red shaded area describes the lower limit for the effective conductivity for the reduced LLCZNO bulk conductivity as discussed in Section 4.2

different porosity. In our analysis, we separate the effect of microstructure and GBs on the conductivity. In the discussion below, we refer to the first case, where only structural effects are taken into account, as effective bulk conductivity (blue). The latter case using our full transport model including GB processes, is shown in red color in Figure 8.

The calculated effective bulk conductivity shows the expected decrease with increasing sample porosity. The effective conductivity reduces up to one order of magnitude for the highly porous sample to  $1.1 \times 10^{-4}$  S/cm. However, deviations to the experimental data are still

another order of magnitude ( $\sim 5.17 \times 10^{-6} \text{ S/cm}$ ).<sup>30</sup>

In contrast, the estimated effective conductivity, including GB processes, shows much better qualitative agreement to our measurements. Notably, the strong decay in conductivity of up to two orders of magnitude of the highly porous sample can be assigned to the increasing GB resistance. As discussed in Section 4.2, the effective ionic conductivity is a result of the superimposition of geometrical constraints, as well as transport limitations through GBs. We observe that the GB resistance provides a significant contribution to the reduction of the ionic conductivity from  $2.1 \times 10^{-4} \text{ S/cm}$  down to  $8.6 \times 10^{-6} \text{ S/cm}$  when going from the dense to the highly porous sample. Still, there is approximately a factor of two between our simulated and the measured effective conductivity. Therefore, we performed some additional simulations using the lower bulk conductivity identified in Section 4.2, which might be a result of lithium evaporation during sintering. The effect of this change in bulk conductivity is given by the red area below the red line and is in excellent agreement with the experimental data.

Note that we did in these calculations not account for the influence of secondary phases on the effective transport properties (cf. Section 4.2). Still, the agreement between simulation and experiment demonstrates that the GB model is able to describe the relevant transport properties of the SE. Therefore in the next section, we investigate the influence of the porous layer transport on the trilayer performance. The change in effective conductivity of the porous SE layer is essential for the following discussion since the lithium transport in the porous SE layer will be a dominating factor for the ASR of the trilayer cells.

#### 4.4 Analysis of Trilayer Cells

In the following section, we extend our simulation study to the galvanostatic operation of virtual trilayer cells. As introduced in Section 2.3, the trilayer structure consists of a dense layer between two porous layers. In our simulations, we use the sample with 56 % porosity, which will provide the most considerable advantage in energy density for future applications.

Degradation of the materials due to lithium evaporation during sintering, such as a reduced bulk conductivity or secondary phases, are neglected in this study. We will specifically focus on the effect of lithium distribution on the ASR of the trilayer. Thereby, we will also analyze the current density distribution and potential hotspots for lithium deposition and dendrite growth. This analysis provides guidelines to identify critical structural features and strategies to mitigate the risk of dendrite formation and cell failure.

#### 4.4.1 Area Specific Resistance

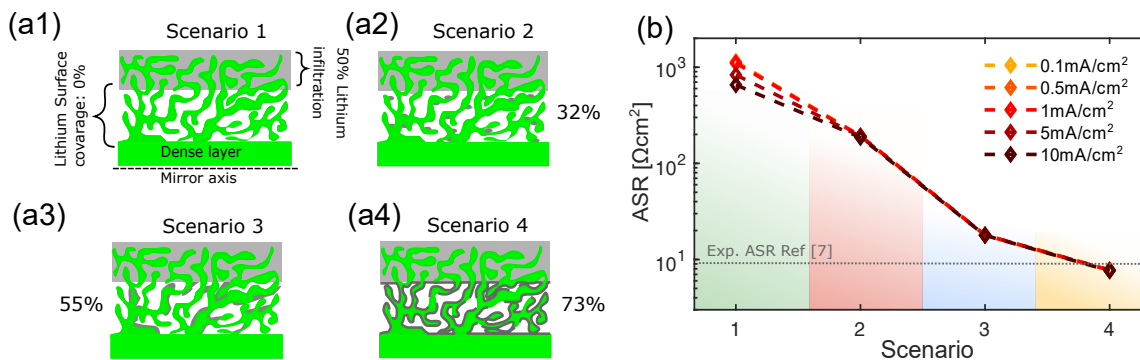


Figure 9: (a) Schematic representation of the four lithium infiltration scenarios investigated for the ASR and the current density distribution of the trilayer framework with 56 % porosity. For all four scenarios, we assume an ideal 50 % filling of both porous electrode sides close to the current collector. The surface coverage of the remaining pore space is gradually increased: (a1) 0 % surface coverage, (a2) 32 % surface coverage, (a3) 55 % surface coverage and (a4) 73 % surface coverage. (b) Calculated ASR for the four different lithiation scenario at different external currents from 0.1 mA/cm<sup>2</sup>-10 mA/cm<sup>2</sup>.

In this paragraph, we analyze the effect of lithium distribution on the ASR. The distributions are chosen to represent different scenarios during galvanostatic cycling of the trilayer cells. The different distributions are generated based on a visual interpretation of SEM images, and a schematic overview of the scenarios is shown in Figure 9 (a1) to (a4). The underlying concept for the lithium plating is a surface closing film growth, starting from the current collector towards the dense layer. This mechanism is accompanied by the formation of extended lithium whiskers branching along the SE surface, cross-linking the remaining lithium islands and subsequently expanding the percolating network.<sup>40</sup> The corresponding

evolution of the ASR is shown in Figure 9 (b).

In our simulations, we start with a configuration in which half of the porous layers close to the current collectors are filled with lithium. This corresponds to an ideal plating and stripping of lithium without additional electronic conductivity provided by the SE or the SE surface coating.<sup>8</sup> In this case, a lithium front moves through the porous layer towards the separator or current collector during plating and stripping, respectively. This scenario is referred to as scenario 1 and is depicted in Figure 9(a1).

For the estimation of the ASR, we apply different currents from 0.1 mA/cm<sup>2</sup>, 0.5 mA/cm<sup>2</sup>, 1 mA/cm<sup>2</sup>, 5 mA/cm<sup>2</sup> up to 10 mA/cm<sup>2</sup>. Note, that the latter corresponds to the highest stripping current reported in literature for this type of system.<sup>7</sup> The corresponding ASRs are shown in Figure 9 (b) and are also listed in Table S5.

In scenario 1 the ASR for all currents fluctuates around 1100  $\Omega\text{cm}^2$ . This is in line with the expected potential drop based on the effective ionic conductivity of the samples and similar values were measured on a non-infiltrated trilayer between planar lithium electrodes.<sup>8</sup> This indicates that most of the ASR is related to the lithium transport in the SE. Moreover, it demonstrates that our model parametrized based on the impedance measurements is able to provide qualitative predictions on the ASR of the porous samples in trilayer configuration. However, the ASR of fully and partially infiltrated samples is reported to be orders of magnitude smaller.<sup>7,8,40</sup> Since most of the ASR is due to lithium transport in the SE, the transport pathways need to be considerably shorter in this case. This indicates additional pathways for electronic conduction, presumably through lithium clusters or deposits, which remain in the porous structure during cycling.

To investigate the effect of residual lithium in the porous layer on ASR, we simulate three additional scenarios with increasing lithium content in the pore space. For the second scenario (Figure 9(a2)) we redistribute  $\sim 3\text{vol} - \%$  lithium in both porous layers of the trilayer setup. This residual lithium covers 32% of the SE surface, yet, it does not form a

percolating conduction network. For scenario 3 and 4 (Figure 9(a3) and (a4)), the residual lithium content in the pore space is increased to 6 % and 10 vol-%, respectively. For scenario 3 an electronically conductive network starts to form (55 % surface coverage). However, a fully percolating network is only established in scenario 4 with a surface coverage of 73 %.

Overall, we observe a decrease of the ASR with increasing lithium surface coverage in the porous SE layers. Even in scenarios 2 and 3 where we did not observe a percolating network, the ASR already decreases to  $\sim 194 \Omega\text{cm}^2$  and  $\sim 17 \Omega\text{cm}^2$ , respectively. Finally, in scenario 4, where the residual lithium film is almost entirely covering the SE surface (73 %), the simulated ASR reduces to  $\sim 7 \Omega\text{cm}^2$ , which is also reported in experiments on similar structures.<sup>7</sup> As indicated by the distribution of local current densities, higher surface coverage reduces the effective length for the transport of lithium ions in the SE (cf. supplementary information S9). In scenario 4 a large fraction of the cell ASR originates due to the dense layer ( $\sim 3.7\text{-}7 \Omega\text{cm}^2$ ). Additionally, the increasing surface coverage promotes a homogeneous distribution of local Faradaic currents by increasing the active surface area and allows for an improved stripping/plating of the metallic lithium. This point is discussed in more detail in the sections below.

However, we underline that in our studies, the contribution of Faradaic processes to the ASR is minor compared to the ionic transport in the SE, indicating that an essential factor for ASR reduction is the optimization of the conductive networks. After the initial thermal infiltration step, the lithium distribution is expected to be more homogeneous, corresponding to scenario 1. Indeed the measured ASR in the initial cycles is higher and then gradually decreases. This is in line with our assumption that lithium clusters like in scenarios 2-4 form in the initial cycles and help to reduce the ASR of the trilayer setup. Therefore, the initial stripping and plating cycles are regarded as important for battery lifetime, and a sufficient lithium infiltration is essential to surpass the large initial ASR due to the low ionic conductivity of the highly porous SE (cf. Figure 8).<sup>7,8</sup>

We expect that the formation of a percolating lithium surface layer inside the SE can be en-

hanced by a functional coating, which improves the wetting behavior between the electrolyte and metallic lithium. The reduced surface tension allows for intimate contact and, therefore, should also increase lithium mobility along the SE surface.<sup>7,8,40</sup> Moreover, recent atomistic calculations on the electronic structure of LLZO indicate a tendency for enhanced lithium deposition on the SE surface due to an increased electron density.<sup>26</sup> Generalizing these findings to LLCZNO, this material characteristic would additionally promote formation of thin percolating surface films during cycling.

Note that in our studies, due to the spatial resolution of virtual samples, the lithium distribution algorithm most likely overestimates the residual lithium content needed for a percolating network. We expect that the formation of conductive surface pathways is possible at a much lower lithium content. Nevertheless, qualitative predictions of our model will not change and additional information on the morphology of lithium deposits at different depths of cycling is needed to confirm our analysis.

#### 4.4.2 Current Density Distribution

The decreasing ASR is an indicator for a reduced local current density inside the trilayer structure. A homogeneous distribution of local currents will in turn be very beneficial for the cycle life of the cells. We use a histogram representation to quantify current densities in the trilayer structure for the four different scenarios shown in Figure 10(a). In addition, the microstructure resolved simulations allow us to spatially resolve the location and corresponding magnitude of the emerging current densities in the SE. To compare the influence of the increased residual lithium on hot spot formation in the SE pore space, we select the two complementary cases at scenario 1 and scenario 4. In Figure 10(b,c) the spatially resolved current density distribution for the two different scenarios at  $0.5 \text{ mA/cm}^2$  are shown. To visualize the internal current hot spots, a threshold of  $0.5 \text{ mA/cm}^2$  was set to show only current densities exceeding the applied external current. We also excluded the current densities

of the infiltrated lithium phase represented by the transparent grayish area.

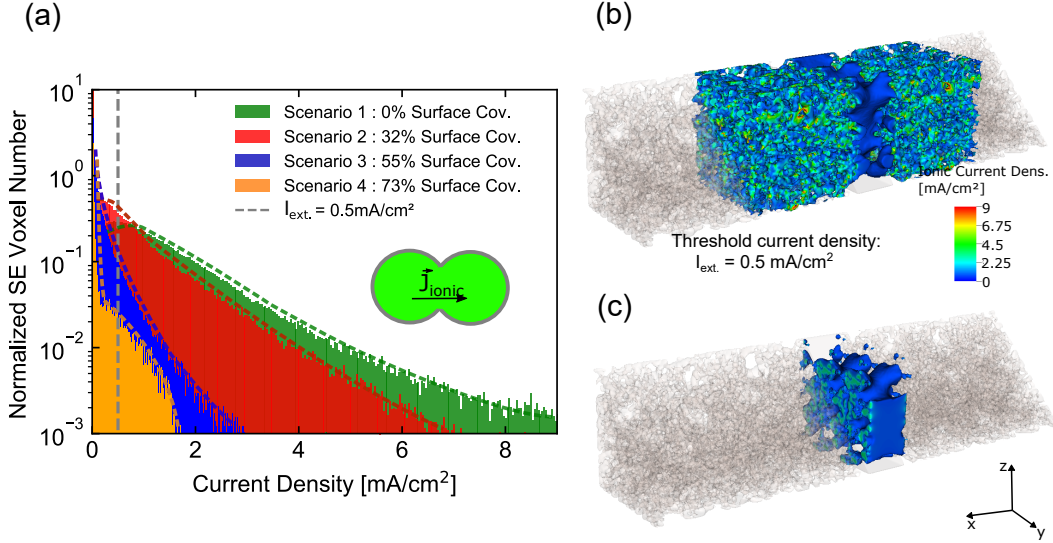


Figure 10: (a) On the left side, the simulated current density distribution inside the SE for varying lithium infiltration scenarios at fixed  $0.5 \text{ mA/cm}^2$  external current (dotted gray): 0 % coverage (green), 32 % coverage (red), 55 % coverage (blue) and 73 % coverage (orange). The histogram distribution is normalized, and the solid black lines are introduced to improve visualization. The included schematic indicates the spatial occurrence of the displayed current densities in the SE structure. On the right side, the respective current density distribution inside the SE phase after setting a threshold of  $I_{ext.} = 0.5 \text{ mA/cm}^2$ : (b) surface coverage 0 % (scenario 1) and (c) surface coverage 73 % (scenario 4).

**Initial Lithium Distribution** Figure 10(a) shows the normalized local ionic current density distribution in the SE for the four lithium distributions. The dotted gray line represents the applied external current density  $I_{ext.} = 0.5 \text{ mA/cm}^2$ . We discard the local current densities of the infiltrated lithium phase for an improved presentation of the data and include additional contour lines for each distribution (dotted black).

All four distributions show a high count of low current densities in the range between  $0-0.1 \text{ mA/cm}^2$ , resulting from the contribution of the SE in contact with the homogeneously infiltrated lithium phase in the porous layers close to the current collector. In scenario 1 (green), without any residual lithium close to the separator, the slight second peak at  $0.5 \text{ mA/cm}^2$  indicates that this type of distribution does not considerably reduce the mean current density in the SE structure. The maximum current density reaches up to  $9 \text{ mA/cm}^2$

and around 73 % of the SE effectively needs to conduct a current which is higher than the applied external current.

The corresponding spatial distribution of local current densities above  $0.5 \text{ mA/cm}^2$  for scenario 1 is shown in Figure 10(b). We see clearly that a significant part of the current flows as lithium ions through the constricted SE volume of the trilayer. As expected, the resulting distribution confirms that for the electrode domains fully infiltrated with lithium (grayish area), the local current reduces due to the increased active surface area of the porous SE. Therefore, we have no significant contributions in the regions close to the current collector. In contrast, the electrode domains close to the dense layer without any lithium on the surface show significant local current densities even way above the applied external current density. We observe distinct hot spots (yellow  $\sim 3 \text{ mA/cm}^2$  and red  $\sim 6 \text{ mA/cm}^2$ ) in the current distribution, which are similar on both sides of the trilayer due to the symmetry of the setup. These hot spots occur predominantly in narrow bottlenecks close to GBs. Thereby, the magnitude of local currents exceeds the applied external current by more than a factor of  $\sim 10$ . However, in the homogeneous dense layer, the current is able to redistribute again. Remarkably, although we do not consider grains and GBs in the dense layer, we see inhomogeneities in the local current density due to the contact with the porous layers.

The estimated high ASR for scenario 1 results from the extremely high local currents in the porous SE structure. Therefore, the low effective ionic conductivity of the SE (cf. Figure 8) is responsible for the major potential drop and gives rise to an increased resistance of the virtual sample similar as it is observed in the initial cycles of the trilayer in the experiments.

**Increasing Lithium Coverage** The current distribution changes for scenario 2 with increased lithium coverage of the SE surface, shown in red color in Figure 10(a). The second peak in the distribution, which is also seen in Scenario 1, shifts below the applied current density. Still, 31 % of the local current density exceeds the applied external current causing a significant increase in ASR. Moreover, the high local currents observed in scenarios 1 and

2 might cause material degradation and the formation of lithium deposits at grain boundaries,<sup>16,23</sup> which is a topic that needs to be revisited in order to understand the impact of local currents on cycle life.

Finally, for scenarios 3 and 4, we see in our simulations a reduction of the mean local current density with a relatively homogeneous distribution across internal surfaces. The resulting current density distributions are displayed in Figure 10(a) in blue and orange color, respectively. With increasing surface coverage, the peak in the distribution shifts further towards lower currents, and the width of the distribution also reduces. For scenario 4, only a minor fraction of the ionic current (1.1 %) exceeds the current applied externally.

This statistical analysis of scenario 4 is illustrated in the corresponding current density distribution shown in Figure 10(c). Elevated currents above  $0.5 \text{ mA/cm}^2$  are only observed close to and inside the dense layer. In general, the distribution of scenario 4 shows a significant decrease in the magnitude of local currents without any hot spots, as seen in scenario 1. Only at the contact between the dense and porous layers isolated spots with slightly increased current are emerging. Nevertheless, through the residual lithium and the increased active surface area, the local current densities and the ASR in the porous SE structure is reduced significantly.

The simulation study confirms that in order to cycle the trilayer structure at elevated discharge currents, a sufficient coverage of the porous SE surface area by metallic lithium is mandatory. Otherwise, the reduced active surface area for the lithium transfer into the SE will lead to prolonged ionic transport pathways, increasing the cell resistance due to the low effective ionic conductivity of the porous layers. The increasing surface coverage in the porous SE enhances the formation of a conductive electronic network, which improves the electrode utilization as well as the cycling performance.<sup>7,8</sup>

Moreover, we identified that at the contact area between the porous SE network and the dense layer as critical for the lithium transport. Since the dense layer also serves as a protect-

ing layer to suppress dendrite formation, the current density distribution in this domain is critical for operation at higher currents. In the following section, we focus on the distribution of the current hot spots inside the trilayer structure at elevated currents.

### 4.4.3 Operation at High Currents

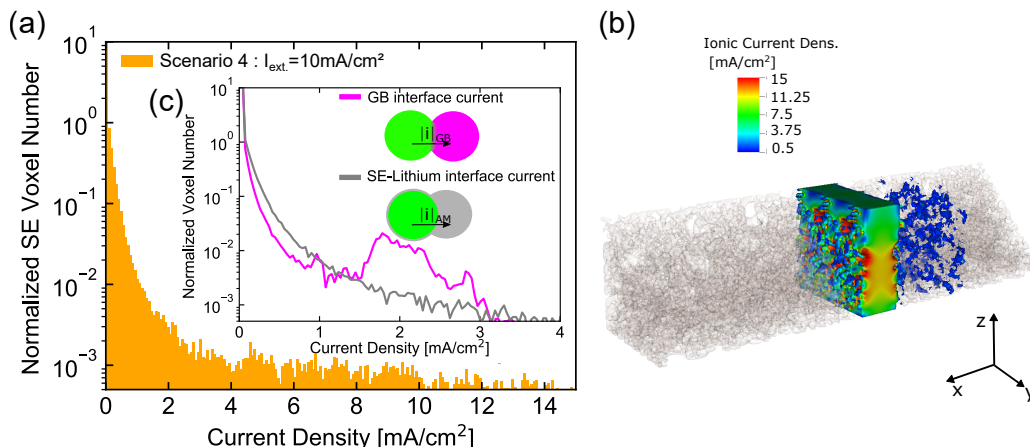


Figure 11: (a) Normalized SE current density distribution for the trilayer structure (scenario 4) at 10 mA/cm<sup>2</sup> external current. (b) Respective spatial current density distribution after applying a  $I_{ext.}=0.5$  mA/cm<sup>2</sup> threshold filter. Inset: (c) Normalized distribution for the estimated interface current densities: GB interface (light green) and SE-lithium interface (gray).

The previous analysis revealed that even though a conductive network of lithium is forming in scenario 4, elevated current densities can be observed inside the dense layer and at the contact points to the porous structure. In the experiments, stable operation of the symmetrical trilayer of 10 mA/cm<sup>2</sup> was achieved.<sup>7</sup> CCD experiments were not conducted so this was not necessarily an upper limit on current density. Instead, after achieving 10 mA/cm<sup>2</sup> the cycling shifted to a lithium depletion test wherein the amount of lithium cycled was increased to the point that it exceeded the volume of lithium in the pores and the corresponding increase in ASR at that point used as confirmation of lack of dendrite shorts. However, distinct spikes in the cell voltage were observed during cycling, indicating sudden changes in the ASR. This fluctuation could point towards non-uniform stripping and plating due to the inhomogeneous current density distribution discussed above. High currents

could amplify inhomogeneities which could cause degradation of the SE as well as ultimately enhance dendrite formation.

As described earlier, a common criterion in this respect is the empirical CCD, which is meant to indicate the highest current density before the cells start to fail. Recent publications suggest that the CCD for garnet-type materials that are wetted by a lithium metal electrode is around  $0.9 \text{ mA/cm}^2$ .<sup>21</sup> Therefore, a dendrite free stripping and plating in the trilayer system can be expected, if the major part of the current density distribution at the lithium interface as well as at the GB and SE interfaces stays below  $0.9 \text{ mA/cm}^2$ . Note that the CCD is a rather empirical concept which is generally sensitive to multiple factors such as the SE thickness, surface area, roughness, and cell configuration. Certainly, additional work is necessary to identify stability windows of the materials and critical local conditions for dendrite formation as function of local material properties. Nevertheless, the CCD concept provides a first estimate for critical conditions, and we select a CCD of  $0.9 \text{ mA/cm}^2$  as an experimentally common test rate for the later analysis of the trilayer.<sup>10</sup> In our discussion, we investigate the current distribution for scenario 4 at elevated external currents to identify limitations of the setup. Figure 11(a) shows the resulting SE current density distribution at  $10 \text{ mA/cm}^2$  external current. The respective 3D current distribution in the trilayer is shown in Figure 11(b). A threshold of  $0.5 \text{ mA/cm}^2$  is set to allow comparison with the current distribution at low currents shown in Figure 10(c). Additionally, we include in the inset in Figure 11(c) the local current density distribution found at the SE-lithium interface (solid gray) and the GB interface (solid pink). These interface currents for the SE-lithium and the GB interface relate to the aforementioned dendrite growth kinetics, namely the internally and externally originating dendrites.

As expected from the previous analysis, a large fraction ( $\sim 96.5\%$ ) of the ionic current density in the SE is below  $0.5 \text{ mA/cm}^2$ , due to the percolating conductive network for electrons in the lithium phase. Still, compared to the low external current case ( $0.5 \text{ mA/cm}^2$ ), we observe an increase in current density contributions above the critical value by a factor

of  $\sim 20$ . Moreover, the distribution becomes broader with a larger share of currents above  $10 \text{ mA/cm}^2$ , and some isolated spots around  $14 \text{ mA/cm}^2$ . A similar trend can also be seen in the distribution of interface currents given in Figure 11(c). Although most of the interfacial current densities stay below the CCD, around 1.5% of the current fraction is still above the critical value. This could potentially accelerate degradation processes in the trilayer cell. In general, both distributions are more narrow compared to the overall SE current density with maximum currents around  $4 \text{ mA/cm}^2$ . This results from the fact that the overall SE ionic current density also includes bulk contributions for all three spatial axis directions of the evaluated voxel.

Note that we observe a peak in GB interface current given in (cf. Figure 11(c)) at around  $2 \text{ mA/cm}^2$ . Our analysis shows that most of the voxels with currents around  $2 \text{ mA/cm}^2$  are close to the dense layer. The increased GB current could trigger the formation of internal dendrites along GBs, which rupture the dense layer. Recent publications suggest that the relatively high electronic conductivity of LLZO compared to other SE would allow for the formation of metallic lithium along GBs even at some distance to the lithium interface.<sup>24,26,65</sup> In order to avoid inhomogeneities in the dense layer, a rational design of the porous layers is needed, which is discussed in the next paragraph.

The 3D current density distribution shown in Figure 11(b) emphasizes that critical currents predominantly occur in the dense layer and in the porous layer where lithium is plated at the SE-lithium interface. The same pattern can also be found in the 3D distribution of GB and SE-lithium interface currents shown in the supplementary information S9. Compared to the lower currents (cf. Figure 10(c)) the number of hot spots as well as the magnitude of the currents increases significantly. Due to the high porosity of the SE electrode, there are only few points in contact with the dense layer. Therefore, the current is highest at these bottlenecks and then reduces in magnitude inside the dense layer (cf. Figure 11(c)). At low external currents, the homogeneous structure of the dense layer is able to redistribute the current after only few micrometer. (cf. Figure 10(b,c)). However, at high currents, we see

that the inhomogeneities propagate through the whole thickness of the dense layer, as seen in Figure 11(b). The currents in these inhomogeneities exceed the applied current density by more than 50% which might increase the risk of material degradation due to undesired lithium plating in the vicinity of the dense layer. Like lithium deposition along the GBs, the inhomogeneous lithium plating at the interface to the dense layer could additionally be an origin of mechanical failure mechanisms of the trilayer structure.

The inhomogeneities also influence the current distribution in the porous layer, causing an asymmetry, despite the lithium distribution in both porous layers being identical. We assume that these asymmetries can cause inhomogeneous stripping of the lithium surface in the porous layers. Eventually, in some pores, lithium can be entirely stripped from the surface, causing a sudden increase in the ASR, which can be seen as a spike in the cell voltage like observed in the experiments at high currents.<sup>7,40,66</sup> Since the ASR reduces in subsequent cycles, the experimental data suggest a reestablishment of the lithium surface covering during cycling, again providing short transport pathways for lithium ions in the SE.

#### 4.4.4 Optimization Strategy

Our studies in the previous paragraph show that the low contact area between porous and dense layer mitigates high local currents and produces inhomogeneous current distribution through the dense layer. Both effects significantly increase the ASR and might trigger additional degradation mechanisms.

To improve the rate performance at elevated currents, we propose a modification of the contact area between the porous and dense layer. By creating an electrode with a gradually decreasing porosity towards the dense layer, one can improve the transport of ions at the dense layer. This structure optimization would provide a more homogeneous distribution of currents, without significantly reducing the pore space for lithium infiltration.

In order to virtually test this approach, we create a trilayer structure with a porous layer

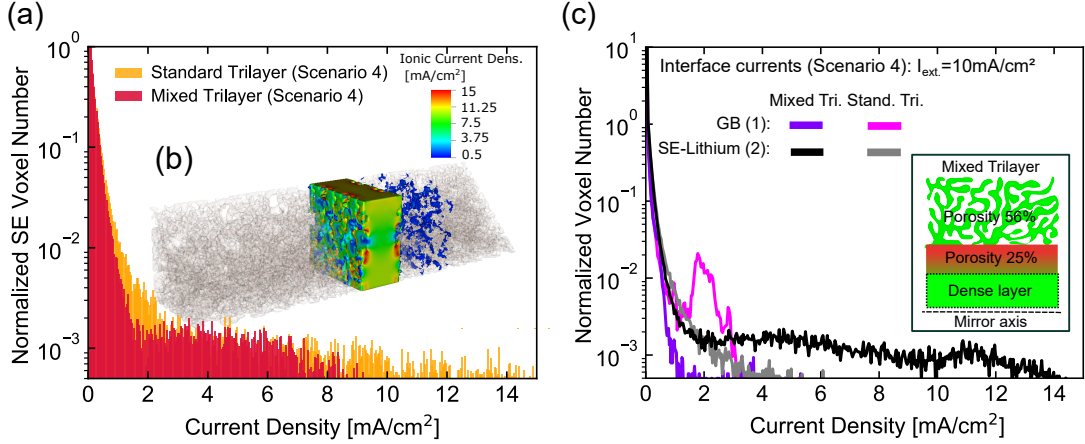


Figure 12: (a) Normalized SE current density distribution for the standard (orange) and mixed (dark red) trilayer cell for infiltration scenario 4 at  $10 \text{ mA/cm}^2$  external current. (b) Spatial current distribution for the mixed trilayer structure after setting a  $0.5 \text{ mA/cm}^2$  threshold. (c) Evolution of the interface current density between standard and mixed trilayer for scenario 4 at  $10 \text{ mA/cm}^2$ . Inset: Schematic for the modified structural design of the mixed trilayer cell.

with a reduced porosity of 25% on both sides of the dense layer (cf. Figure 12(c)). The  $7 \mu\text{m}$  thick layer is on one side in intimate contact with the dense layer to improve the ionic transport. On the other side, it is connected with the highly porous layer (56%), which provides the necessary pore space for high energy applications.

Figure 12(a) shows current density histograms of the standard (orange) and the mixed trilayer (dark red) setup for an external current of  $10 \text{ mA/cm}^2$ . In both structures, we use a lithium distribution following scenario 4. The corresponding 3D SE current density distribution of the mixed trilayer is shown in Figure 12(b). In addition, the distribution of interface currents for the GB and SE-lithium interface are given in Figure 12(c).

Figure 12(a) shows a histogram of ionic current in the electrolyte. The graph shows that the suggested modified trilayer geometry (dark red) provides a more homogeneous distribution and significantly reduces the maximum current compared to the standard (orange) electrode. For the mixed trilayer design, the overall fraction exceeding  $0.5 \text{ mA/cm}^2$  decreases by 30%, which results in an ASR reduction of  $\sim 4.3 \Omega\text{cm}^2$  ( $-30\%$ ). This reduction can also be linked to the decrease in GB interface current, given by the pink line in Figure 12(c). Remarkably,

we see that the peak at around  $2 \text{ mA/cm}^2$  observed for the standard trilayer setup (pink) decreases significantly in the mixed trilayer design (violet). This proves that the lower porosity optimize the transition of lithium ions from the porous to the dense layer. Therefore, the mixed design might be less prone to internal dendrite formation. Moreover, we observe an improved redistribution of the current density, potentially enabling a more stable cycling at higher currents and consequently reduce the experimentally observed voltage spikes.

Still, the reduction of pore space close to the dense layer results in a corresponding rise of the SE-lithium interface current due to the reduced lithium contact area, as shown in Figure 12(c) (solid black). The fraction of interface current above  $0.5 \text{ mA/cm}^2$  increases by a factor of 4 compared to the standard electrode. Still, overall the fraction is on a relatively low level. Moreover, we assume that unless the dense layer show any pin holes or significant structural surface defects, the mechanical integrity of the dense layer is sufficient to avoid the penetration due to externally originating dendrites.<sup>8</sup> Therefore, we believe that the benefits of the mixed design such as the reduction of the ASR and the homogenized ionic current distribution in the dense layer more than compensate the higher SE-lithium interface currents. Still, more studies on the mechanisms of dendrite formation<sup>8,24,65</sup> in this specific setup are needed to prove our assumptions.

Overall the optimization study emphasizes that a porosity gradient in the porous layers provides a possible route to improve the trilayer performance.<sup>7</sup> Nevertheless, additional experimental studies are needed to test the predicted improvements for the ASR and cycling stability as well as explore possible processing routes.

## 5 Conclusions

In this work, we present microstructure resolved continuum simulations of LLCZNO samples with varying porosity. A special feature of our model is that it describes the transport of lithium across grains and grain boundaries in the solid electrolyte network. The simulation

studies are performed on reconstructions of LLCZNO samples obtained by FIB-SEM measurements. For the parametrization and validation of our model, we simulate electrochemical impedance spectra and compare them to the corresponding measurements. This approach allows us to correlate structural features of the reconstructions such as SE porosity, grain boundary density, and secondary phases, with characteristic features in the impedance spectra. Our simulations indicate that highly porous samples are prone to lithium evaporation, reducing the bulk and or grain boundary conductivity and eventually might be responsible for the formation of secondary phases with very low lithium conductivity. The latter can be identified by a second feature in the impedance spectra and is most prominently observed for the highly porous sample. Moreover, we confirmed that the effective ionic conductivity is controlled by the electrode porosity, which affects the constriction of the lithium transport pathways as well as the contribution of the grain boundaries. Simulated effective conductivities are in excellent agreement with the experimental data providing the basis for our design study of the so-called trilayer setup.

In a first step, we analyze the ASR of trilayer cells for various lithium distributions, reproducing potential infiltration scenarios during galvanostatic cycling of the cells. The analysis shows that a percolating conductive lithium network is needed for a low ASR as it is observed in the experiments. Only in this case, stable cycling at high rates will be possible. Furthermore, we performed a detailed analysis of the spatial distribution of local current densities. Our analysis demonstrates that the trilayer setup significantly reduces local currents. However, we identify local hot-spots in the current distribution at the interface between the porous and dense layers, which cause a very inhomogeneous current distribution at high currents. These inhomogeneities increase the ASR and also the risk for degradation processes. Therefore, we propose a modified trilayer structure with a gradually decreasing porosity towards the dense layer. The virtually designed electrode shows an improved current density distribution as well as a drastically reduced ASR, insinuating a more stable cycling behavior at elevated currents.

The computational studies presented in this work provide an analysis of physical and electrochemical processes limiting the performance of the trilayer design, representing a promising cell concept for ASSBs. Based on our simulations, we are able to suggest strategies for the design of the next generation of trilayer cells. Still, fundamental questions such as the influence of grain boundary properties and composition on the effective SE conductivity need to be addressed. Especially, taking into account effects like lithium loss during processing, since a fundamental understanding and tailoring of structural and grain boundary properties will be essential to further improve oxide-based SE for future ASSBs.

## Acknowledgement

This work was conducted as part of the US-German joint collaboration on "Interfaces and Interphases In Rechargeable Li-metal based Batteries" supported by the US Department of Energy (DOE) and German Federal Ministry of Education and Research (BMBF). Financial support from the BMBF within the 03XP0223E and DOE under grant number DEEE0008858. The authors acknowledge support with computational resources provided by the state of Baden-Württemberg through bwHPC (bwForCluster JUSTUS).

## Supporting Information Available

The following files are available free of charge.

- Supporting information: additional experimental information on cell assembly ,and symmetric impedance data; FIB-SEM image data; additional simulation results; model parametrization equations

## References

- (1) Dunn, B.; Kamath, H.; Tarascon, J. M. Electrical energy storage for the grid: A battery of choices. *Science* **2011**, *334*, 928–935.
- (2) Covert, T.; Greenstone, M.; Knittel, C. R. Will we ever stop using fossil fuels? *Journal of Economic Perspectives* **2016**, *30*, 117–138.
- (3) Murugan, R.; Thangadurai, V.; Weppner, W. Schnelle Lithiumionenleitung in granatartigem  $\text{Li}_7\text{La}_3\text{Zr}_2\text{O}_{12}$ . *Angewandte Chemie* **2007**, *119*, 7925–7928.
- (4) Xu, K. Nonaqueous liquid electrolytes for lithium-based rechargeable batteries. *Chemical Reviews* **2004**, *104*, 4303–4417.
- (5) Wang, C.; Fu, K.; Kammampata, S. P.; McOwen, D. W.; Samson, A. J.; Zhang, L.; Hitz, G. T.; Nolan, A. M.; Wachsman, E. D.; Mo, Y.; Thangadurai, V.; Hu, L. Garnet-Type Solid-State Electrolytes: Materials, Interfaces, and Batteries. *Chemical Reviews* **2020**, *120*, 4257–4300.
- (6) Zhang, B.; Tan, R.; Yang, L.; Zheng, J.; Zhang, K.; Mo, S.; Lin, Z.; Pan, F. Mechanisms and properties of ion-transport in inorganic solid electrolytes. *Energy Storage Materials* **2018**, *10*, 139–159.
- (7) Hitz, G. T.; McOwen, D. W.; Zhang, L.; Ma, Z.; Fu, Z.; Wen, Y.; Gong, Y.; Dai, J.; Hamann, T. R.; Hu, L.; Wachsman, E. D. High-rate lithium cycling in a scalable trilayer Li-garnet-electrolyte architecture. *Materials Today* **2019**, *22*, 50–57.
- (8) Yang, C.; Zhang, L.; Liu, B.; Xu, S.; Hamann, T.; McOwen, D.; Dai, J.; Luo, W.; Gong, Y.; Wachsman, E. D.; Hu, L. Continuous plating/stripping behavior of solid-state lithium metal anode in a 3D ion-conductive framework. *Proceedings of the National Academy of Sciences* **2018**, *115*, 3770–3775.

- (9) Han, X.; Gong, Y.; Fu, K. K.; He, X.; Hitz, G. T.; Dai, J.; Pearse, A.; Liu, B.; Wang, H.; Rubloff, G.; Mo, Y.; Thangadurai, V.; Wachsman, E. D.; Hu, L. Negating interfacial impedance in garnet-based solid-state Li metal batteries. *Nature Materials* **2016**, *16*, 572–579.
- (10) Porz, L.; Swamy, T.; Sheldon, B. W.; Rettenwander, D.; Frömling, T.; Thaman, H. L.; Berendts, S.; Uecker, R.; Carter, W. C.; Chiang, Y.-M. Mechanism of Lithium Metal Penetration through Inorganic Solid Electrolytes. *Advanced Energy Materials* **2017**, *7*, 1701003.
- (11) Krauskopf, T.; Dippel, R.; Hartmann, H.; Peppler, K.; Mogwitz, B.; Richter, F. H.; Zeier, W. G.; Janek, J. Lithium-Metal Growth Kinetics on LLZO Garnet-Type Solid Electrolytes. *Joule* **2019**, *3*, 2030–2049.
- (12) Miao, X.; Wang, H.; Sun, R.; Wang, C.; Zhang, Z.; Li, Z.; Yin, L. Interface engineering of inorganic solid-state electrolytes for high-performance lithium metal batteries. *Energy & Environmental Science* **2020**, *13*, 3780–3822.
- (13) Tsai, C. L.; Ma, Q.; Dellen, C.; Lobe, S.; Vondahlen, F.; Windmüller, A.; Grüner, D.; Zheng, H.; Uhlenbruck, S.; Finsterbusch, M.; Tietz, F.; Fattakhova-Rohlfing, D.; Buchkremer, H. P.; Guillon, O. A garnet structure-based all-solid-state Li battery without interface modification: Resolving incompatibility issues on positive electrodes. *Sustainable Energy and Fuels* **2019**, *3*, 280–291.
- (14) Finsterbusch, M.; Danner, T.; Tsai, C. L.; Uhlenbruck, S.; Latz, A.; Guillon, O. High Capacity Garnet-Based All-Solid-State Lithium Batteries: Fabrication and 3D-Microstructure Resolved Modeling. *ACS Applied Materials and Interfaces* **2018**, *10*, 22329–22339.
- (15) Cheng, L.; Wu, C. H.; Jarry, A.; Chen, W.; Ye, Y.; Zhu, J.; Kostecki, R.; Persson, K.; Guo, J.; Salmeron, M.; Chen, G.; Doeff, M. Interrelationships among Grain Size, Surface

- Composition, Air Stability, and Interfacial Resistance of Al-Substituted Li<sub>7</sub>La<sub>3</sub>Zr<sub>2</sub>O<sub>12</sub> Solid Electrolytes. *ACS Applied Materials and Interfaces* **2015**, *7*, 17649–17655.
- (16) Flatscher, F.; Philipp, M.; Ganschow, S.; Wilkening, H. M. R.; Rettenwander, D. The natural critical current density limit for Li<sub>7</sub>La<sub>3</sub>Zr<sub>2</sub>O<sub>12</sub> garnets. *Journal of Materials Chemistry A* **2020**, *8*, 15782–15788.
- (17) Krauskopf, T.; Hartmann, H.; Zeier, W. G.; Janek, J. Toward a Fundamental Understanding of the Lithium Metal Anode in Solid-State Batteries - An Electrochemo-Mechanical Study on the Garnet-Type Solid Electrolyte Li<sub>6.25</sub>Al<sub>0.25</sub>La<sub>3</sub>Zr<sub>2</sub>O<sub>12</sub>. *ACS Applied Materials and Interfaces* **2019**, *11*, 14463–14477.
- (18) Yang, C.; Liu, B.; Jiang, F.; Zhang, Y.; Xie, H.; Hitz, E.; Hu, L. Garnet/polymer hybrid ion-conducting protective layer for stable lithium metal anode. *Nano Research* **2017**, *10*, 4256–4265.
- (19) Zhou, W.; Zhu, Y.; Grundish, N.; Sen Xin,.; Wang, S.; You, Y.; Wu, N.; Gao, J.; Cui, Z.; Li, Y.; Goodenough, J. B. Polymer lithium-garnet interphase for an all-solid-state rechargeable battery. *Nano Energy* **2018**, *53*, 926–931.
- (20) Fu, K.; Gong, Y.; Hitz, G. T.; McOwen, D. W.; Li, Y.; Xu, S.; Wen, Y.; Zhang, L.; Wang, C.; Pastel, G.; Liu, B.; Xie, H.; Yao, Y.; Wachsman, E.; Hu, L. Three-dimensional bilayer garnet solid electrolyte based high energy density lithium metal-sulfur batteries. *Energy and Environmental Science* **2017**, *10*, 1568–1575.
- (21) Taylor, N. J.; Stangeland-Molo, S.; Haslam, C. G.; Sharafi, A.; Thompson, T.; Wang, M.; Garcia-Mendez, R.; Sakamoto, J. Demonstration of high current densities and extended cycling in the garnet Li<sub>7</sub>La<sub>3</sub>Zr<sub>2</sub>O<sub>12</sub> solid electrolyte. *Journal of Power Sources* **2018**, *396*, 314–318.
- (22) Xu, B.; Li, W.; Duan, H.; Wang, H.; Guo, Y.; Li, H.; Liu, H. Li<sub>3</sub>PO<sub>4</sub>-added garnet-type

- Li<sub>6.5</sub>La<sub>3</sub>Zr<sub>1.5</sub>Ta<sub>0.5</sub>O<sub>12</sub> for Li-dendrite suppression. *Journal of Power Sources* **2017**, *354*, 68–73.
- (23) Tsai, C. L.; Roddatis, V.; Chandran, C. V.; Ma, Q.; Uhlenbruck, S.; Bram, M.; Heitjans, P.; Guillon, O. Li<sub>7</sub>La<sub>3</sub>Zr<sub>2</sub>O<sub>12</sub> Interface Modification for Li Dendrite Prevention. *ACS Applied Materials and Interfaces* **2016**, *8*, 10617–10626.
- (24) Han, F.; Westover, A. S.; Yue, J.; Fan, X.; Wang, F.; Chi, M.; Leonard, D. N.; Dudney, N. J.; Wang, H.; Wang, C. High electronic conductivity as the origin of lithium dendrite formation within solid electrolytes. *Nature Energy* **2019**, *4*, 187–196.
- (25) Song, Y.; Yang, L.; Tao, L.; Zhao, Q.; Wang, Z.; Cui, Y.; Liu, H.; Lin, Y.; Pan, F. Probing into the origin of an electronic conductivity surge in a garnet solid-state electrolyte. *Journal of Materials Chemistry A* **2019**, *7*, 22898–22902.
- (26) Tian, H.-K.; Liu, Z.; Ji, Y.; Chen, L.-Q.; Qi, Y. Interfacial Electronic Properties Dictate Li Dendrite Growth in Solid Electrolytes. *Chemistry of Materials* **2019**, *31*, 7351–7359.
- (27) Manalastas, W.; Rikarte, J.; Chater, R. J.; Brugge, R.; Aguadero, A.; Buannic, L.; Llordés, A.; Aguesse, F.; Kilner, J. Mechanical failure of garnet electrolytes during Li electrodeposition observed by in-operando microscopy. *Journal of Power Sources* **2019**, *412*, 287–293.
- (28) Yu, S.; Siegel, D. J. Grain Boundary Contributions to Li-Ion Transport in the Solid Electrolyte Li<sub>7</sub>La<sub>3</sub>Zr<sub>2</sub>O<sub>12</sub> (LLZO). *Chemistry of Materials* **2017**, *29*, 9639–9647.
- (29) Fu, K. K.; Gong, Y.; Liu, B.; Zhu, Y.; Xu, S.; Yao, Y.; Luo, W.; Wang, C.; Lacey, S. D.; Dai, J.; Chen, Y.; Mo, Y.; Wachsman, E.; Hu, L. Toward garnet electrolyte-based Li metal batteries: An ultrathin, highly effective, artificial solid-state electrolyte/metallic Li interface. *Science Advances* **2017**, *3*, 1–12.

- (30) Hamann, T.; Zhang, L.; Gong, Y.; Godbey, G.; Gritton, J.; McOwen, D.; Hitz, G.; Wachsman, E. The Effects of Constriction Factor and Geometric Tortuosity on Li-Ion Transport in Porous Solid-State Li-Ion Electrolytes. *Advanced Functional Materials* **2020**, *1910362*, 1910362.
- (31) Yang, C.; Zhang, L.; Liu, B.; Xu, S.; Hamann, T.; McOwen, D.; Dai, J.; Luo, W.; Gong, Y.; Wachsman, E. D.; Hu, L. Continuous plating/stripping behavior of solid-state lithium metal anode in a 3D ion-conductive framework. *Proceedings of the National Academy of Sciences* **2018**, 201719758.
- (32) Latz, A.; Zausch, J. Multiscale modeling of lithium ion batteries: Thermal aspects. *Beilstein Journal of Nanotechnology* **2015**, *6*, 987–1007.
- (33) Braun, S.; Yada, C.; Latz, A. Thermodynamically Consistent Model for Space-Charge-Layer Formation in a Solid Electrolyte. *Journal of Physical Chemistry C* **2015**, *119*, 22281–22288.
- (34) Hein, S.; Danner, T.; Westhoff, D.; Prifling, B.; Scurtu, R.; Kremer, L.; Hoffmann, A.; Hilger, A.; Osenberg, M.; Manke, I.; Wohlfahrt-Mehrens, M.; Schmidt, V.; Latz, A. Influence of Conductive Additives and Binder on the Impedance of Lithium-Ion Battery Electrodes: Effect of Morphology. *Journal of The Electrochemical Society* **2020**, *167*, 013546.
- (35) Danner, T.; Singh, M.; Hein, S.; Kaiser, J.; Hahn, H.; Latz, A. Thick electrodes for Li-ion batteries: A model based analysis. *Journal of Power Sources* **2016**, *334*, 191–201.
- (36) Schmitt, T.; Latz, A.; Horstmann, B. Derivation of a local volume-averaged model and a stable numerical algorithm for multi-dimensional simulations of conversion batteries. *Electrochimica Acta* **2020**, *333*, 135491.
- (37) Neumann, A.; Randau, S.; Becker-Steinberger, K.; Danner, T.; Hein, S.; Ning, Z.; Marrow, J.; Richter, F. H.; Janek, J.; Latz, A. Analysis of Interfacial Effects in All-

- Solid-State Batteries with Thiophosphate Solid Electrolytes. *ACS Applied Materials and Interfaces* **2020**, *12*, 9277–9291.
- (38) GeoDict by Math2Market, commercial software for structure analysis and generation. <https://www.math2market.com/?Language=de>, Accessed: 2019-09-18.
- (39) Baychev, T. G.; Jivkov, A. P.; Rabbani, A.; Raeini, A. Q.; Xiong, Q.; Lowe, T.; Withers, P. J. *Transport in Porous Media*; Springer Netherlands, 2019; Vol. 128; pp 271–301.
- (40) Xu, S.; McOwen, D. W.; Wang, C.; Zhang, L.; Luo, W.; Chen, C.; Li, Y.; Gong, Y.; Dai, J.; Kuang, Y.; Yang, C.; Hamann, T. R.; Wachsman, E. D.; Hu, L. Three-Dimensional, Solid-State Mixed Electron-Ion Conductive Framework for Lithium Metal Anode. *Nano Letters* **2018**, *18*, 3926–3933.
- (41) Randau, S.; Weber, D. A.; Kötz, O.; Koerver, R.; Braun, P.; Weber, A.; Ivers-Tiffée, E.; Adermann, T.; Kulisch, J.; Zeier, W. G.; Richter, F. H.; Janek, J. Benchmarking the performance of all-solid-state lithium batteries. *Nature Energy* **2020**, *5*, 259–270.
- (42) BEST by Fraunhofer ITWM, commercial software for 3D resolved battery simulation. [https://www.itwm.fraunhofer.de/content/dam/itwm/de/documents/SMS\\_Infomaterial/sms\\_flyer\\_BEST\\_EN.pdf](https://www.itwm.fraunhofer.de/content/dam/itwm/de/documents/SMS_Infomaterial/sms_flyer_BEST_EN.pdf), Accessed: 2019-09-18.
- (43) Latz, A.; Zausch, J. Thermodynamic derivation of a Butler-Volmer model for intercalation in Li-ion batteries. *Electrochimica Acta* **2013**, *110*, 358–362.
- (44) Becker-Steinberger, K.; Schardt, S.; Horstmann, B.; Latz, A. Statics and Dynamics of Space-Charge-Layers in Polarized Inorganic Solid Electrolyte, to be published.
- (45) Wu, J. F.; Guo, X. Origin of the low grain boundary conductivity in lithium ion conducting perovskites:  $\text{Li}_{3x}\text{La}_{0.67-x}\text{TiO}_3$ . *Physical Chemistry Chemical Physics* **2017**, *19*, 5880–5887.

- (46) Wu, J. F.; Guo, X. Size effect in nanocrystalline lithium-ion conducting perovskite:  $\text{Li}_{0.30}\text{La}_{0.57}\text{TiO}_3$ . *Solid State Ionics* **2017**, *310*, 38–43.
- (47) Hongahally Basappa, R.; Ito, T.; Morimura, T.; Bekarevich, R.; Mitsuishi, K.; Yamada, H. Grain boundary modification to suppress lithium penetration through garnet-type solid electrolyte. *Journal of Power Sources* **2017**, *363*, 145–152.
- (48) Mei, A.; Wang, X. L.; Lan, J. L.; Feng, Y. C.; Geng, H. X.; Lin, Y. H.; Nan, C. W. Role of amorphous boundary layer in enhancing ionic conductivity of lithium-lanthanum-titanate electrolyte. *Electrochimica Acta* **2010**, *55*, 2958–2963.
- (49) Haase, R. and Thermodynamics for Any Number and Kind By. **1982**, 1–7.
- (50) Rettenwander, D.; Wagner, R.; Reyer, A.; Bonta, M.; Cheng, L.; Doeff, M. M.; Limbeck, A.; Wilkening, M.; Amthauer, G. Interface instability of fe-stabilized  $\text{Li}_7\text{La}_3\text{Zr}_2\text{O}_{12}$  versus li metal. *Journal of Physical Chemistry C* **2018**, *122*, 3780–3785.
- (51) Zhu, Y.; Connell, J. G.; Tepavcevic, S.; Zapol, P.; Garcia-Mendez, R.; Taylor, N. J.; Sakamoto, J.; Ingram, B. J.; Curtiss, L. A.; Freeland, J. W.; Fong, D. D.; Markovic, N. M. Dopant-Dependent Stability of Garnet Solid Electrolyte Interfaces with Lithium Metal. *Advanced Energy Materials* **2019**, *9*, 1–11.
- (52) Wang, C.; Gong, Y.; Liu, B.; Fu, K.; Yao, Y.; Hitz, E.; Li, Y.; Dai, J.; Xu, S.; Luo, W.; Wachsman, E. D.; Hu, L. Conformal, Nanoscale ZnO Surface Modification of Garnet-Based Solid-State Electrolyte for Lithium Metal Anodes. *Nano Letters* **2017**, *17*, 565–571.
- (53) Luo, W.; Gong, Y.; Zhu, Y.; Li, Y.; Yao, Y.; Zhang, Y.; Fu, K. K.; Pastel, G.; Lin, C. F.; Mo, Y.; Wachsman, E. D.; Hu, L. Reducing Interfacial Resistance between Garnet-Structured Solid-State Electrolyte and Li-Metal Anode by a Germanium Layer. *Advanced Materials* **2017**, *29*, 1–7.

- (54) Bian, Z.; Zhu, J.; Wang, J.; Xiao, S.; Nuckolls, C.; Li, H. Multitemplates for the hierarchical synthesis of diverse inorganic materials. *Journal of the American Chemical Society* **2012**, *134*, 2325–2331.
- (55) Thompson, T.; Sharafi, A.; Johannes, M. D.; Huq, A.; Allen, J. L.; Wolfenstine, J.; Sakamoto, J. A tale of two sites: On defining the carrier concentration in Garnet-based ionic conductors for advanced Li batteries. *Advanced Energy Materials* **2015**, *5*, 1–9.
- (56) Ishiguro, K.; Nemori, H.; Sunahiro, S.; Nakata, Y.; Sudo, R.; Matsui, M.; Takeda, Y.; Yamamoto, O.; Imanishi, N. Ta-Doped  $\text{Li}_7\text{La}_3\text{Zr}_2\text{O}_{12}$  for Water-Stable Lithium Electrode of Lithium-Air Batteries. *Journal of The Electrochemical Society* **2014**, *161*, A668–A674.
- (57) Hofstetter, K.; Samson, A. J.; Dai, J.; Gritton, J. E.; Hu, L.; Wachsman, E. D.; Thangadurai, V. Electrochemical Stability of Garnet-Type  $\text{Li}_7\text{La}_{2.75}\text{Ca}_{0.25}\text{Zr}_{1.75}\text{Nb}_{0.25}\text{O}_{12}$  with and without Atomic Layer Deposited- $\text{Al}_2\text{O}_3$  under  $\text{CO}_2$  and Humidity. *Journal of The Electrochemical Society* **2019**, *166*, A1844–A1852.
- (58) Markel, V. A. Introduction to the Maxwell Garnett approximation: tutorial. *Journal of the Optical Society of America A* **2016**, *33*, 1244.
- (59) Wachter-Welzl, A.; Wagner, R.; Rettenwander, D.; Taibl, S.; Amthauer, G.; Fleig, J. Microelectrodes for local conductivity and degradation measurements on Al stabilized  $\text{Li}_7\text{La}_3\text{Zr}_2\text{O}_{12}$  garnets. *Journal of Electroceramics* **2017**, *38*, 176–181.
- (60) Rettenwander, D.; Welzl, A.; Cheng, L.; Fleig, J.; Musso, M.; Suard, E.; Doeff, M. M.; Redhammer, G. J.; Amthauer, G. Synthesis, Crystal Chemistry, and Electrochemical Properties of  $\text{Li}_{7-2x}\text{La}_3\text{Zr}_2\text{O}_{12-x}\text{Mox}$  ( $x = 0.1-0.4$ ): Stabilization of the Cubic Garnet Polymorph via Substitution of  $\text{Zr}^{4+}$  by  $\text{Mo}^{6+}$ . *Inorganic Chemistry* **2015**, *54*, 10440–10449.

- (61) West, A.; Irvine, J.; Sinclair, D. Electroceramics : Characterization by Impedance Spectroscopy. *Advanced Materials* **1990**, *2*, 132–138.
- (62) Sharafi, A.; Haslam, C. G.; Kerns, R. D.; Wolfenstine, J.; Sakamoto, J. Controlling and correlating the effect of grain size with the mechanical and electrochemical properties of  $\text{Li}_7\text{La}_3\text{Zr}_2\text{O}_{12}$  solid-state electrolyte. *Journal of Materials Chemistry A* **2017**, *5*, 21491–21504.
- (63) Fleig, J.; Maier, J. The impedance of ceramics with highly resistive grain boundaries: Validity and limits of the brick layer model. *Journal of the European Ceramic Society* **1999**, *19*, 693–696.
- (64) Yang, K. Y.; Wang, J. W.; Fung, K. Z. Roles of lithium ions and La/Li-site vacancies in sinterability and total ionic conduction properties of polycrystalline  $\text{Li}_{3x}\text{La}_{2/3-x}\text{TiO}_3$  solid electrolytes (0.21  $\leq x \leq$  0.50). *Journal of Alloys and Compounds* **2008**, *458*, 415–424.
- (65) Chen, Y. T.; Jena, A.; Pang, W. K.; Peterson, V. K.; Sheu, H. S.; Chang, H.; Liu, R. S. Voltammetric Enhancement of Li-Ion Conduction in Al-Doped  $\text{Li}_{7-x}\text{La}_3\text{Zr}_2\text{O}_{12}$  Solid Electrolyte. *Journal of Physical Chemistry C* **2017**, *121*, 15565–15573.
- (66) Kasemchainan, J.; Zekoll, S.; Spencer Jolly, D.; Ning, Z.; Hartley, G. O.; Marrow, J.; Bruce, P. G. Critical stripping current leads to dendrite formation on plating in lithium anode solid electrolyte cells. *Nature Materials* **2019**, *18*, 1105–1111.

# Graphical TOC Entry

